ADA278903

The Pennsylvania State University

The Graduate School

THE AERODYNAMIC AND HEAT TRANSFER EFFECTS

OF AN ENDWALL BOUNDARY LAYER FENCE

IN A 90° TURNING SQUARE DUCT
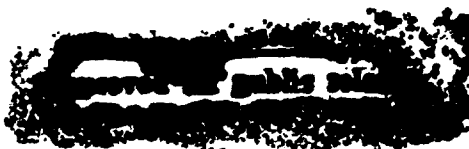
A Thesis in

Aerospace Engineering

by

Dean H. Rizzo

Submitted in Partial Fulfillment
of the Requirements
for the Degree of

Master of Science

May 1994

94 5 04 041

DTIC Q
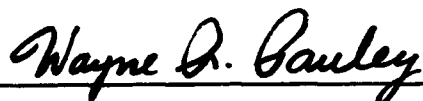
We approve the thesis of Dean H. Rizzo.

Date of Signature

_____   3/14 / 1994
Cengiz Camci
Associate Professor of Aerospace Engineering
Thesis Advisor

_____   3/21/94
Wayne R. Pauley
Assistant Professor of Aerospace Engineering

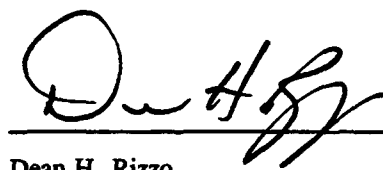_____   3/21/94
Dennis K. McLaughlin
Professor of Aerospace Engineering
Head of the Department of Aerospace Engineering

I grant The Pennsylvania State University the nonexclusive right to use this work for the University's own purposes and to make single copies of the work available to the public on a not-for-profit basis if copies are not otherwise available.

Dean H. Rizzo

ABSTRACT

This experimental study investigates the utility of boundary layer fences in turbine passage flow. Boundary layer fences have recently been reintroduced as a possible method to achieve favorable effects in turbines. Previous studies have used linear cascades which necessarily introduce a horseshoe vortex resulting from the endwall boundary layer impinging on the blade leading edge. The present study uses a curved square duct that exhibits no horseshoe vortex, but does have the characteristic passage vortices of a turning flow. The turbine passage is simulated to study the interaction effects of the boundary layer fence and the passage flow dominated by the passage vortices. Specifically, a single boundary layer fence of varying dimensions is attached to a heated endwall of the duct. The flow is fully turbulent at the inlet of the duct. Five-hole probe and liquid crystal thermography experimental techniques are used to determine the changes in the aerodynamic flowfield and the heat transfer coefficient of the heated endwall as compared to the same duct with no fence. Hotwire measurements are also presented for the description of the inlet flow field turbulence.

This study adds to the currently small volume of information on fences in passage flow in several important aspects. The effect of the fence on the passage vortex is studied in a known flow configuration. Extensive flowfield mapping was completed in the same duct and presented in Wiedner and Camci (1993b). The increased pressure losses of thicker (wider) fences are investigated and results show a significant dependence on fence dimensions. Liquid crystal thermography is used to obtain a high-resolution map of the endwall heat transfer coefficient for two fence configurations. The region of maximum heat transfer in both fence cases coincides with the downwash region of a pair of counter rotating vortices formed between the fence and suction surface near the endwall. This information is critical to those interested in application of a fence in actual turbine temperature fields where cooling of the passage surfaces is a real concern. A thin fence extending from 0° to 90° at a distance halfway between suction and pressure surfaces on the endwall is shown to effectively reduce secondary flow by interfering with the passage vortex. The height of the thin fence is approximately half of the inlet boundary layer thickness. A fence of these dimensions and position reduces total pressure loss across the duct 90° plane as compared to the no-fence case. Thicker fences produce varying amounts of additional total pressure loss depending on fence length and height. The reduced secondary flow near the endwall is shown to affect the level of endwall heat transfer rather than its distribution.

TABLE OF CONTENTS

LIST OF FIGURES

LIST OF TABLES

NOMENCLATURE

C = Celsius temperature scale

C_{pt} = total pressure coefficient = $(P_{t,in,cl}-P_t)/.5\rho U^2_{in,cl}$

C_{ps} = static pressure coefficient = $(P-P_{in,cl})/.5\rho U^2_{in,cl}$

C_{ske} = secondary kinetic energy coefficient = $(V^2+W^2)/U^2_{in,cl}$

D = duct width; (m)

HSI = hue, saturation, intensity

h = heat transfer coefficient; (W/m²K)

k = thermal conductivity; (W/mK)

P = local static pressure; (N/m²)

$\dot{q}$ = heatflux; (W/m²)

Q = total mean velocity

rms = root mean square

R_i,R_o = duct inner and outer radius; (m)

Re_D = Reynolds number based on duct width = UD/ν

R35C1W = liquid crystal with approximate color bandwidth of 1°C starting at 35°C

T = mean temperature; (°C)

Tu = turbulence intensity = rms(u')/(U*100)

U_{95} = uncertainty based on 95% coverage

U,V,W = mean velocity components; (m/s)

u',v',w' = fluctuating velocity components; (m/s)

X = streamwise direction

Y = radial direction

Z = spanwise direction

α = pitch angle

β = yaw angle

δ_{99} = boundary layer thickness @ $U/U_{in,cl}=.99$; (mm)

ρ = density; (kg/m³)

ν = kinematic viscosity; (m²/s)

$\omega_x,\omega_y,\omega_z$ = mean vorticity components; (s)⁻¹

Ω = total mean vorticity; (s)⁻¹

Subscripts

a = ambient (outside duct)

cl = duct centerline

cond = conductive

conv = convective

gen = generated

in = inlet

rad = radiative

s = static

t = total or stagnation

w = wall

∞ = freestream (inside duct)

Superscript

— = passage averaged or as defined

ACKNOWLEDGMENTS

I sincerely believe that this project would not have been possible without the help of the Lord, with whom all things are possible. He set down the laws of nature that give purpose and meaning to ̲ience and engineering. I praise Him for His faithfulness and wonder.

I thank my advisor, Professor C. Camci, for establishing an outstanding teaching environment using research in its proper role at an academic institution. He has provided a great example for this student through many stimulating conversations and his inquisitive teaching style.

I thank my fellow graduate students in the Turbomachinery Lab for making graduate school more than just an academic experience. Their help, humor, and humility were truly inspiring.

I cannot thank my wife enough for her unquestionable devotion and love. Lastly, I thank my children, Tricia, Andy, Beth, and Catherine, for their patience. I hope that one day they will read this and know what their Dad did when he "went to school".

Chapter 1
INTRODUCTION

The benefits of increasing the gas-turbine efficiency by only a few tenths of a percent are still very attractive. A common method to achieve higher efficiency is to increase turbine inlet temperature. This method dictates increased coolant effectiveness or increasing the temperature limits of the turbine structural materials. The importance of knowing the heat transfer levels and distribution on turbine passage surfaces is significant. Minimizing coolant flow by putting it where it's needed reduces costly design iterations and decreases durability problems due to hot spots. Another method of increasing the turbine efficiency is reducing the pressure losses by reducing secondary flow. The three-dimensional flowfield present in the turbine has been adequately visualized to capture the complex interaction of many factors such as turbulence, pressure gradient, passage vortices, and horseshoe vortices (Langston et al. 1977, Langston 1980, Sieverding 1985). However, complete understanding of the role of each of these factors in aerodynamic losses is not evidenced in current prediction methods (Sharma and Butler 1987, Mayle 1991). This investigation deals with the effort to reduce loss due to secondary flow and its effect on the heat load to the passage endwall surface.

Modern gas turbines are low aspect ratio and the entire blade-to-blade passage contains strong secondary flow features. This study uses a large scale, curved square duct to simulate the turbine passage without introducing the characteristic horseshoe vortices of cascade studies. Extensive flowfield mapping of the duct was presented in Wiedner and Camci (1993b) and showed counter-rotating passage vortices dominating the duct flow. The inlet Reynolds number based on duct width is 3.6 x 10^5 and the inlet boundary layer is completely turbulent to more closely simulate actual turbine conditions. A single boundary layer fence is attached to one endwall of the duct in an effort to reduce the passage vortex flow along the endwall. The dimensions of the fence (length, height, and width) are varied, but all are placed at the mid-passage location between suction and pressure surfaces. The effects of the fence on the flowfield and aerodynamic losses are measured using a five-hole probe in the 90° plane of the duct. Several fence configurations having significant impact on secondary flow near the heated endwall are then used to study the effects on heat transfer to the endwall. Liquid crystal thermography is used to obtain a high-resolution map of the convective heat transfer coefficient for the entire endwall. Comparisons of aerodynamic flowfield and endwall heat transfer are made with the same duct with no fence installed.

Chapter 2

RELATED INVESTIGATIONS

The idea of using boundary layer fences for positive aerodynamic effect is not a recent one. Fences were used in the 1950's on swept back wings of jet fighter aircraft to prevent the stalling of the wing at the tip due to the thickening boundary layer. The boundary layer was thicker at the wingtip due to the pressure gradient on the suction side forcing boundary layer fluid toward the tip. Prumper (1972) reported that boundary layer fences installed on the hub and casing walls in turbomachinery might reduce losses; however, he did not present any data on the amount of loss reduction (Kawai et al., 1989). Unpublished work at Pratt & Whitney by Langston included installation of a fence on the airfoil suction surface in a cascade (Sharma and Graziani, 1983). Langston's work showed that a fence reduced the movement of fluid from the region near the endwall toward the midspan region of the suction surface.

Several recent studies have focused specifically on aerodynamic effects of endwall boundary layer fences in turbine cascades. Kawai et al. (1989) used very thin (.5mm) fences of varying height and position on both endwalls of a turbine rotor cascade with $Re_c=4.5x10^5$. They report a 22% reduction in secondary losses compared to the no-fence cascade using the optimum fence configuration. They found the optimum configuration was thin fences located on both endwalls midway between blades extending from inlet to exit with height equal to 1/3 of the inlet boundary layer thickness. They report that the passage averaged total pressure loss between inlet and exit is reduced by 10% for the same fence configuration. Interestingly, they report that fences of $.5(\delta_{99})_{in}$ or greater height do not decrease passage secondary loss compared to the no-fence cascade. They report the same trend for total pressure loss. Conversely, they report that passage averaged secondary kinetic energy is reduced by all fence configurations. They report this reduction in loss is closely related to "capturing" the pressure side leg of the horseshoe vortex above the fence, thus, not allowing it to increase the strength of the passage vortex.

More recently, Chung et al. (1991) used a triangular-shaped endwall fence in a cascade to prevent the pressure-side leg of the horseshoe vortex from washing film-cooling flow off the blade suction surface. They used flow visualization at $Re_c=2.93x10^5$ and fence height of 11.3 mm. The inlet boundary layer thickness was not reported. They report reduced aerodynamic losses and improved cooling performance due to the fence effects on the passage vortex. Chung and Simon (1993) further investigated endwall boundary layer fences at increased freestream turbulence levels (Tu=10%). They concluded that the passage vortex still dominates, the fence still reduces the strength of the vortex, and the fence may still reduce aerodynamic losses in the passage. The present study differs from these past fence studies primarily by isolating the effects of the fence on the passage vortex without the horseshoe vortex.

Taylor et al. (1982) investigated laminar and turbulent flow in a square duct of the same radius ratio

as the present study and found that inlet boundary layer thickness significantly affects secondary velocity magnitude in the first 30° of the bend and that the influence diminished by 60° in the bend. They conclude that turbulent flow is dominated by the acceleration of the core in the first 45° due to the streamwise pressure gradient.

Boyle et al. (1988) made a detailed comparison of secondary flow in a vane cascade and curved duct. They report that the two flows are very similar with two exceptions. The effects of the horseshoe vortex in the cascade are limited to the leading edge/endwall junction and the secondary flow is stronger in the duct passage (thus greater viscous loss). They found the secondary flow in both geometries is dominated by a passage vortex. The vortex moves low-momentum fluid in the endwall boundary layers from pressure to suction sides and eventually onto the suction surface where a characteristic high-loss core displaces the primary flow. Boyle and Hoose (1989) compared the endwall heat transfer in a vane cascade and curved duct. They report that the dominant features of the heat transfer coefficient distribution on the duct endwall are qualitatively the same as the cascade endwall except in the leading edge region due to higher heat transfer associated with the horseshoe vortex and that the heat transfer values were consistently larger in the duct due to the stronger passage vortex.

There are numerous studies of endwall heat transfer in a cascade over the past twenty years. Resolution of the heat transfer distribution has improved continuously as experimental techniques have progressed from discrete thermocouple studies to those using the heat-mass transfer analogy or liquid crystals. Increased resolution is important because of the complex nature of the flow. Many investigators have shown a relationship between enhanced endwall heat transfer and secondary flow phenomena. Graziani et al. (1980), Gregory-Smith et al. (1988) and Boyle and Russell (1990) all conclude that inlet boundary layer thickness affects endwall heat transfer levels, but not the distribution. Hippensteele and Russell (1988) and Boyle and Russell (1990) have investigated Reynolds number effects on endwall heat transfer and clearly demonstrated the high resolution of the liquid crystal technique. A map of the endwall heat transfer in a vane cascade by Goldstein and Spores (1988) using the heat-mass transfer analogy shows that convective heat transfer increases 31% average over the flat plate case. Fisher and Eibeck (1990) found that a longitudinal vortex can enhance turbulent convective heat transfer 23% - 50% over a flat plate in some cases. Pauley and Eaton (1988) investigated the aerodynamic and heat transfer effects of pairs of streamwise vortices in a turbulent boundary layer. They report that the major mean effects of the vortex pairs are the thickening of the boundary layer where the secondary flow is directed away from the wall (upwash) and thinning where the flow is toward the wall (downwash). They found that heat transfer modification is strongly dependent on vortex interaction and that a counter-rotating pair of vortices can enhance net heat transfer. Also, they conclude that the downwash region of a vortex is characterized by elevated levels of peak turbulence intensity and that the turbulence intensity near the wall plays a key role in determining the rate of heat transfer.

Chapter 3

TEST FACILITY, INSTRUMENTATION, AND PROCEDURE

3.1. Facility Description

The experimental test section and reference coordinate system are depicted in Figure 1. An example fence configuration is shown in Figure 1 to orient the reader. The aerodynamic and heat transfer data were obtained in the same duct. The entire duct is constructed using plexiglass with endwall surfaces 12.7 mm thick and pressure and suction surfaces 4.76 mm thick. The duct has a radius ratio, $R_r=(R_i+R_o)/2D$, of 2.3 and square cross-section of $D=203$ mm. A heat transfer composite surface made of a thin foil (Inconel 600, .0254 mm thick) and covered by black paint and several layers of encapsulated chiral nematic liquid crystals (R35C1W) is built on one endwall, Figure 2. The Inconel foil extends from 508 mm upstream of 0° to 20 mm downstream of 90° as shown in Figure 1. Copper bus bars are attached to the foil at upstream and downstream ends to apply the voltage drop and ensure a boundary condition of uniform potential. A variable current DC power supply is connected to the bus bars to generate resistive heating in the Inconel foil. Four k-type, thin-film thermocouples are attached to the surface of the foil (under the paint and liquid crystals) using double-sided tape that is thermally conductive, but electrically insular. The thermocouples are used for liquid crystal calibration. Two 500 watt incandescent lamps are used for illumination during calibration and experiment. A probe access slot is cut in the unheated endwall at 90° and lined with sponge foam to minimize pressure loss. The test section inlet is connected downstream of an open-loop wind tunnel consisting of axial fan, screened diffuser, plenum chamber, high area-ratio circular nozzle, circular to square transition nozzle, and constant cross-section duct, Figure 3.

3.2 Fence Configurations

Two thicknesses (widths) of rectangular-shaped boundary layer fences were constructed. "Thick" boundary layer fences are 4.7 mm wide and made of two strips of plexiglass glued together to maintain a 90° arc. A "thin" fence is 1.0 mm wide and made of stainless steel for rigidity. All fences are thermally insulated on the bottom to minimize conduction from the endwall to the fence. All fence leading and trailing edges are tapered and the top surfaces are beveled. Six different fence configurations were used: four thick-fence configurations of varying height and length, one thin-fence configuration, and the baseline no-fence case. All fences were placed on the heated endwall midway between pressure and suction surfaces using the same attachment points, Figure 4. "Full-length" fences extended from 0° to 90° and "half-length" fences extended from 45° to 90°. "Full-height" fences were approximately equal to the inlet boundary layer thickness (25.4 mm) and "half-height" fences measured 12.7 mm.

- NOT to scale
- D = 20.3 cm
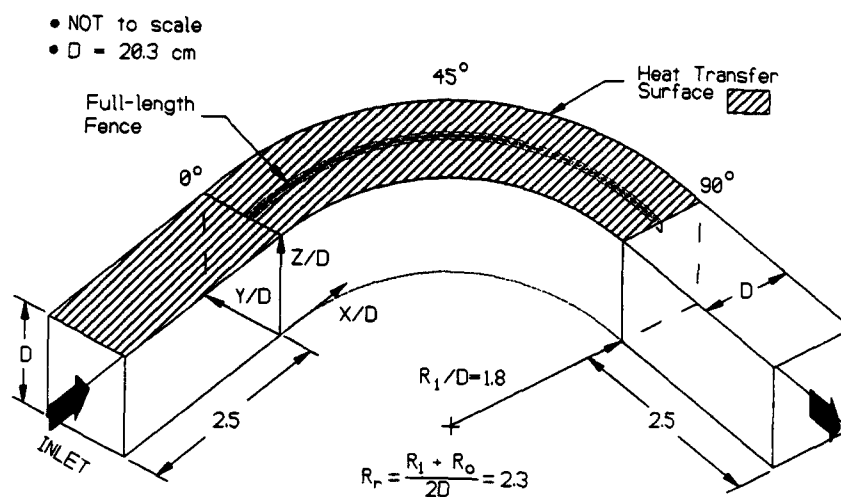
Figure 1: 90° duct with reference coordinate system
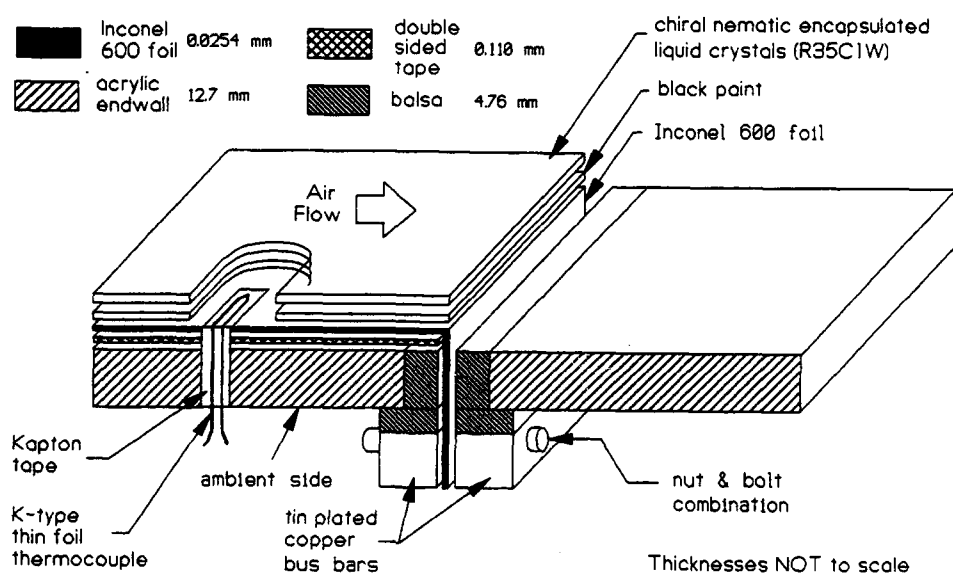
Figure 2: Endwall heat transfer composite surface
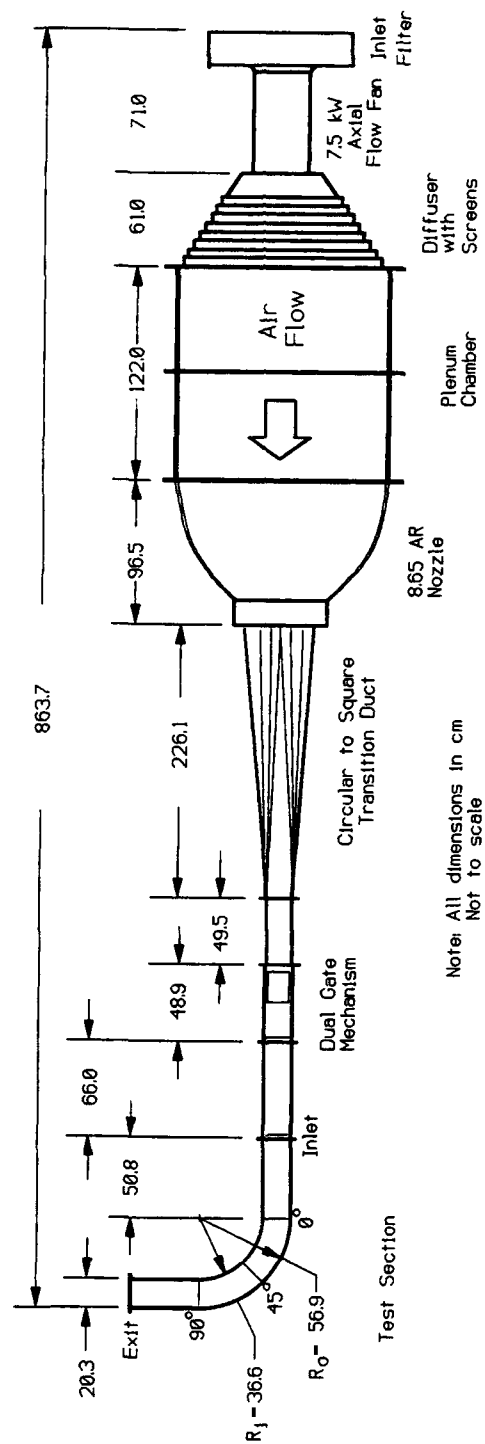
Figure 3: Wind tunnel facility with 90° bend test section
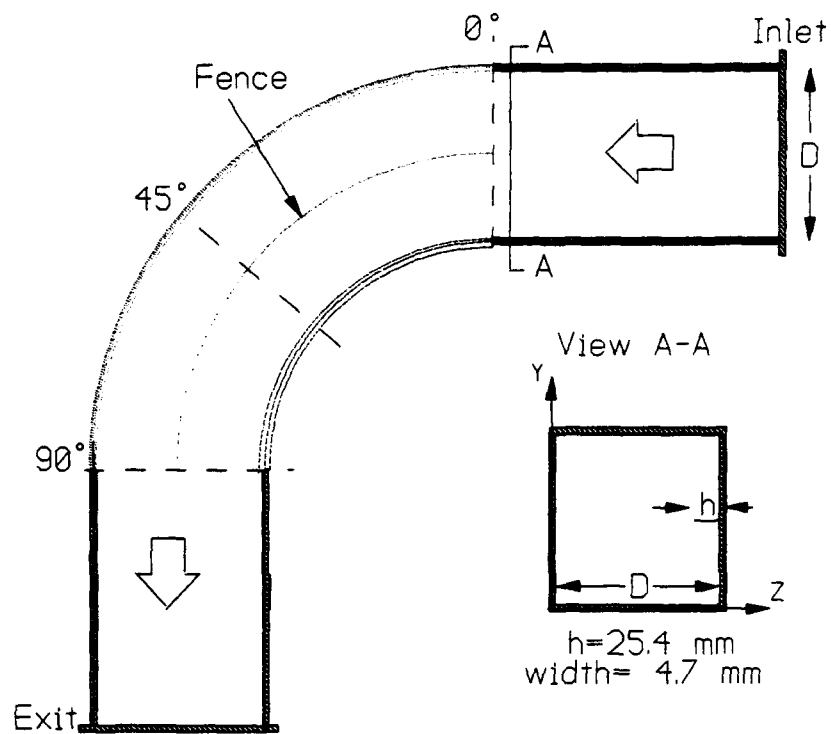
(a) 4.7 mm wide, full-length, full-height fence
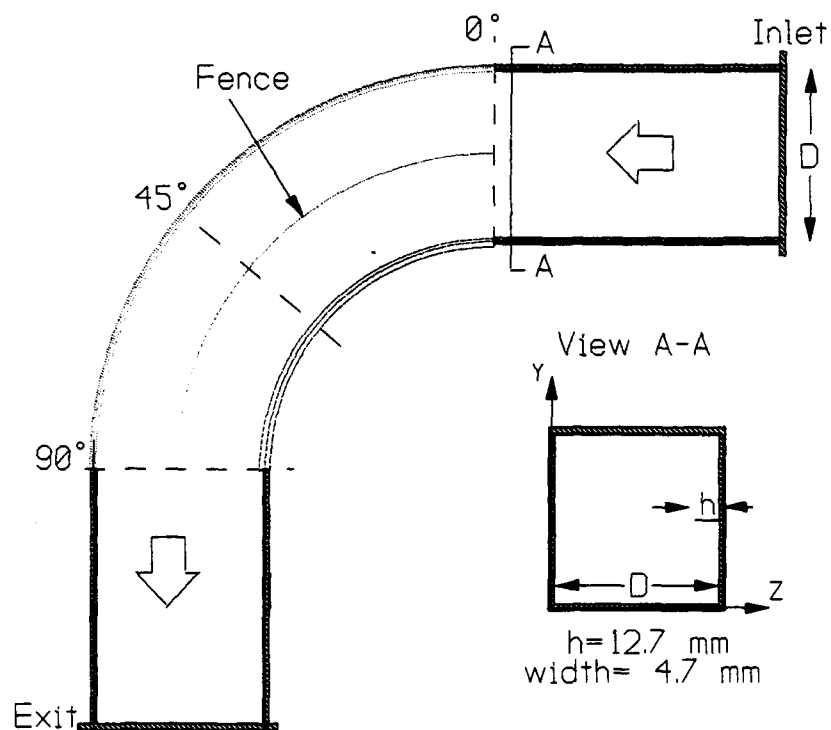
(b) 4.7 mm wide, full-length, half-height fence

Figure 4: 90° duct with fence configurations   (cont. on next page)
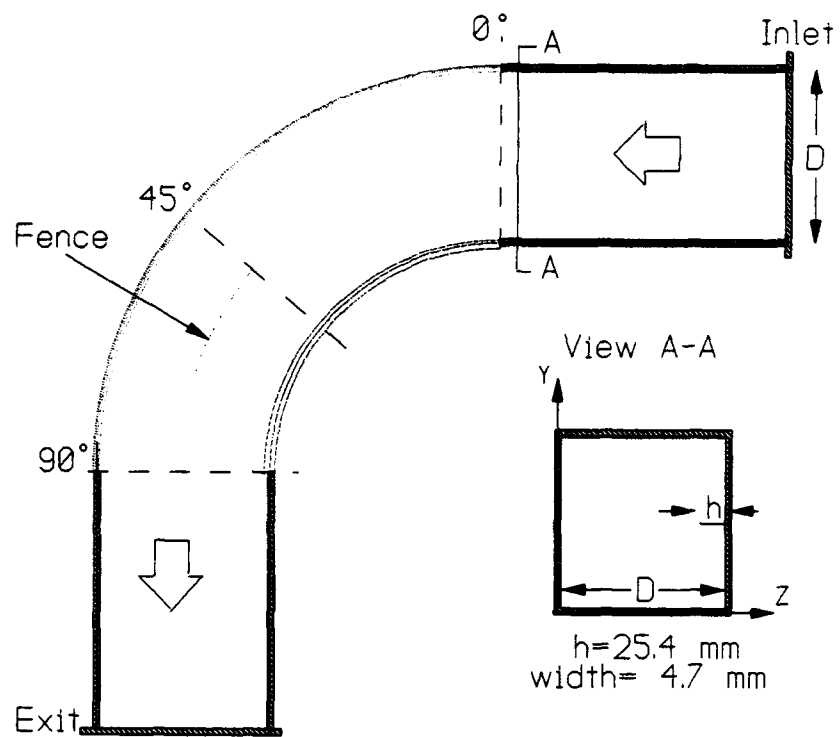
(c) 4.7 mm wide, half-length, full-height fence

(d) 4.7 mm wide, half-length, half-height fence

Figure 4: (cont.)

(e) 1.0 mm wide, full-length, half-height fence

(f) no fence

Figure 4: (cont.)

3.3. Aerodynamic Measurements

The figures displaying aerodynamic information are organized to show the fence cases in always the same order. Figure xx(a) always represents the 4.7 mm wide, full-length, full-height case and Figure xx(b) always represents the 4.7 mm wide, full-length, half-height case. This order continues for all six fence configurations, cases (a) through (f). Figures displaying heat transfer information are individually titled.

3.3.1. Five-hole Probe Description and Data Acquisition

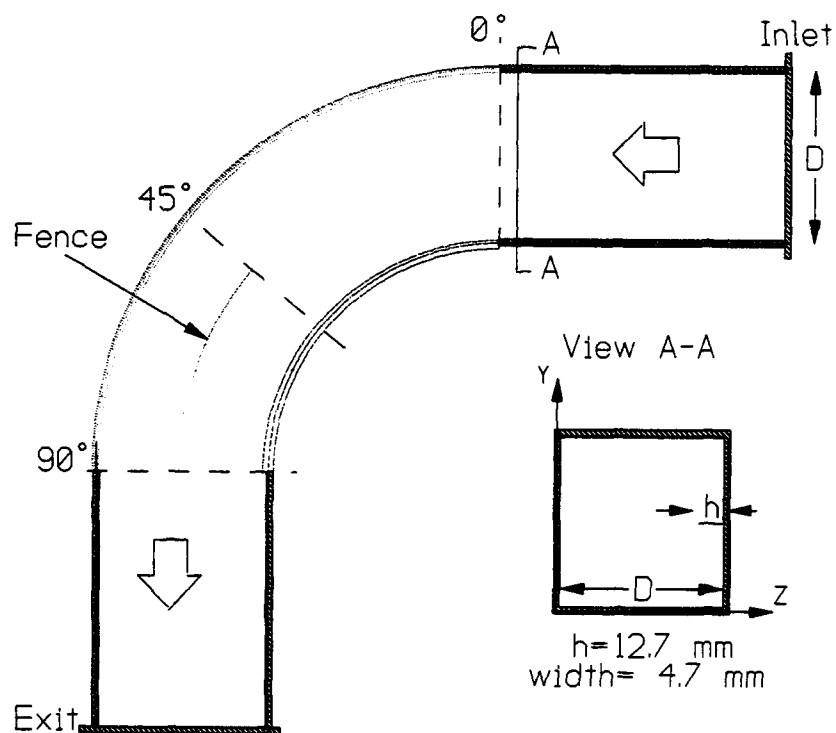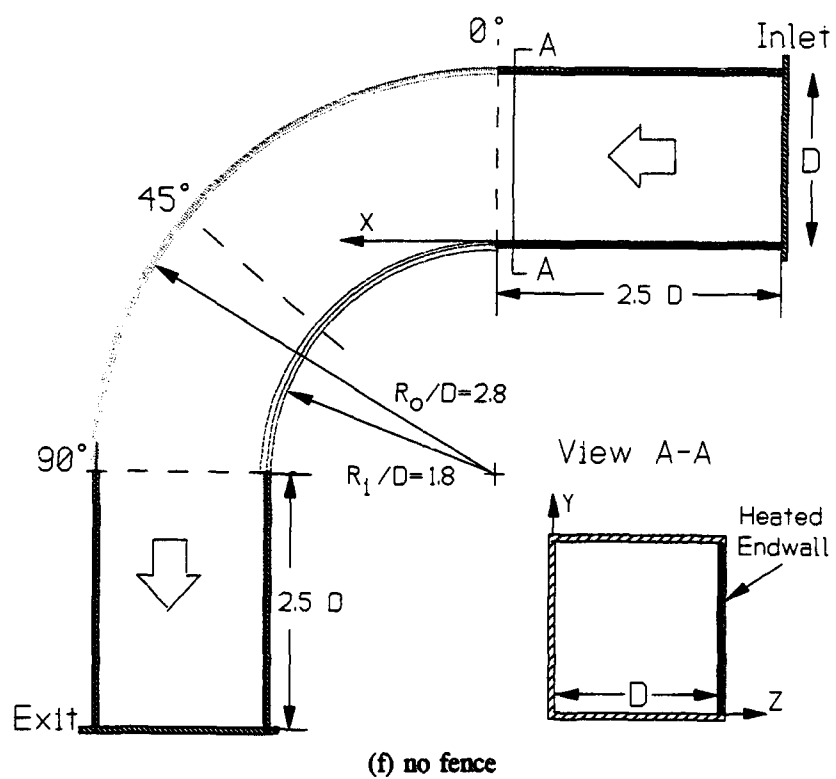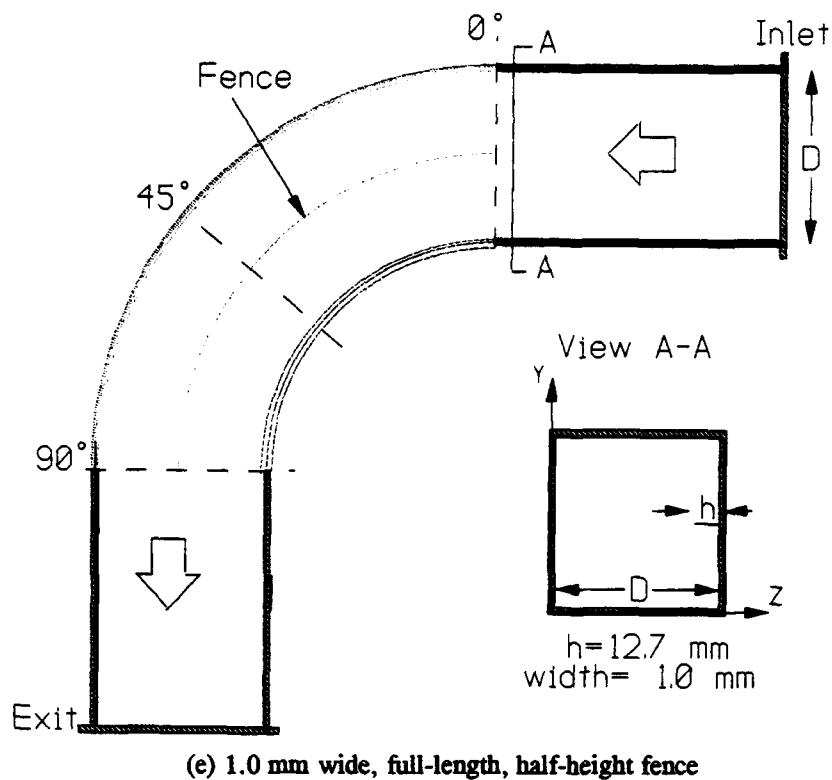A five-hole probe was used to determine the mean velocity vector (all three components and direction), total and static pressure. No fluctuating components of velocity or pressure were measured. The five-hole probe consists of four holes placed symmetrically around a fifth center hole as shown in Figure 5. The four outside holes are inclined 45° to the center hole. The small probe diameter, 1.68 mm, minimizes spatial error in the presence of velocity and pressure gradients. The five tubes at the probe head are enclosed in a shaft for stability while traversing in the flowfield. These tubes are connected to a five-channel, differential pressure transducer through flexible tubing. The orientation of each pressure tube to the flow is shown in Figure 5. The five-hole probe was locally designed and manufactured.

Each channel of the five-channel pressure transducer was separately connected to a six-channel signal demodulator. The demodulator allows offset and amplification adjustment to the analog signal from the transducers. The offset was controlled by the 'zero' trimpot on the demodulator and was used to adjust the analog signal between -2.5 V and +2.5 V. The amplification (or gain) of the analog signal was controlled by the 'span' trimpot and was used to ensure maximum resolution of the pressure range seen in the actual flow. Thus, the offset and amplification of each signal were different due to the nature of the flow in the duct (e.g. channel 1 would measure a greater range in pressure than channel 4) and due to the individual characteristics of each channel. The five-channel pressure transducer and six-channel signal demodulator were designed and manufactured locally by a fellow graduate student. The demodulator output signal was sent to a analog-to-digital (A/D) converter and sampled at a high rate. The A/D data acquisition system was Model DAS-16 from Metrabyte, Inc. There were 1000 digital samples taken over a 4 second period and time averaged. This occurred simultaneously for each channel and the results recorded in a datafile.

The five-hole probe was placed in the duct through an access slot cut in the unheated endwall. The slot was filled with sponge foam to minimize pressure loss. The probe was moved by an electro-mechanical traversing mechanism. Small, direct-current stepping motors turned long screws attached to the probe support platform. The stepping motors were digitally controlled through a controller-driver device that ensured very accurate placement of the probe. The measurement grid was 5 mm from the duct surfaces to minimize wall interference effects. The entire process of probe traversing and data acquisition was controlled by a personal computer using software written locally in TurboPascal language. Aerodynamic measurements were obtained for a 30 x 30 grid at the 90° plane for each of the six fence configurations.
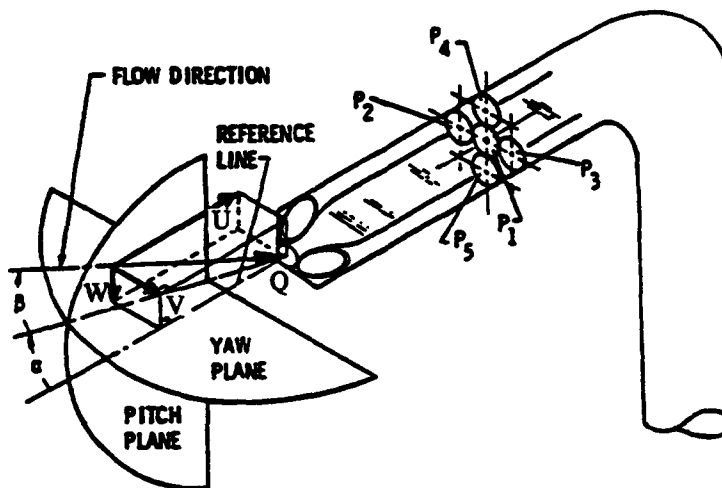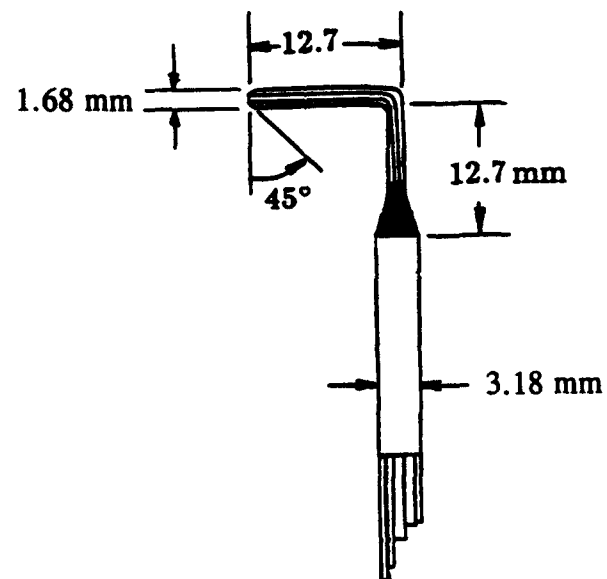
Figure 5: Five-hole probe and reference coordinate system

3.3.2. Calibration

Calibration of all data acquisition components for the five-hole probe was completed in two separate calibrations. The pressure transducers were calibrated using a manometer in place of the five-hole probe. The pressure transducers' signals were demodulated and sampled by the same equipment as the actual data to reduce the sources of error in the measured values. Calibration itself reduces bias uncertainty, but not precision. The transducers were calibrated in the pressure range 0"-2" H$_2$O based on the inlet dynamic pressure (.5ρU^2) of approximately 2.1" H$_2$O. The calibration data points were plotted voltage vs. pressure as depicted in sample pressure transducer calibration plots shown in Figure 6. Linear regression was used to obtain the slope and constant offset for each probe channel. Eight repetitions of the calibration in varying ambient temperature and pressure conditions over a five-month period showed that the calibration slope changed very little ($\pm$.5%) and that only the constant offset changed with changing ambient conditions. Thus, the value for each channel at zero pressure was recorded (as part of the computer code) prior to and after each experimental test to determine the constant offset for each pressure transducer channel used in data reduction.

The five-hole probe was calibrated in the non-nulled mode in the large uniform flow area at the inlet to the duct using the method of Treaster and Yocum (1979). The five-hole probe was connected to the calibrated pressure-transducers and the signal was demodulated and sampled just as the actual data. The calibration map of pitch (α) and yaw (β) pressure coefficients (C$_{p,pitch}$ and C$_{p,yaw}$) was determined experimentally for the range -30 to +30 degrees, Figure 7(a). The probe was calibrated in the pitch-yaw mode (first rotation was in pitch plane) at the test case Reynolds number. The pressure coefficients were computed according to Equations 3.1, 3.2, and 3.3.

$$C_{p,yaw} = \frac{P_3 - P_2}{P_1 - \overline{P}} \tag{3.1}$$

$$C_{p,pitch} = \frac{P_4 - P_5}{P_1 - \overline{P}} \tag{3.2}$$

$$\overline{P} = \frac{1}{4}(P_2 + P_3 + P_4 + P_5) \tag{3.3}$$

The calibration maps of C$_{p,static}$ vs. pitch angle and C$_{p,total}$ vs. pitch angle, Figure 7(b) and 7(c), were determined using static and total pressures measured with a pitot static probe at the same location. The pressure coefficients were computed according to Equations 3.4 and 3.5.
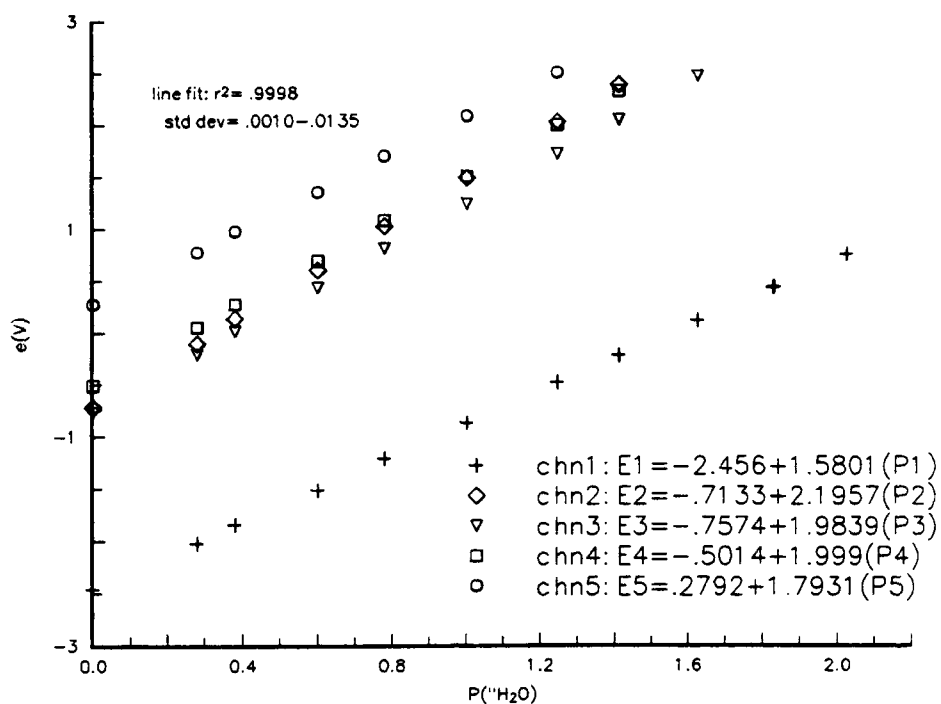
(a) September 1993
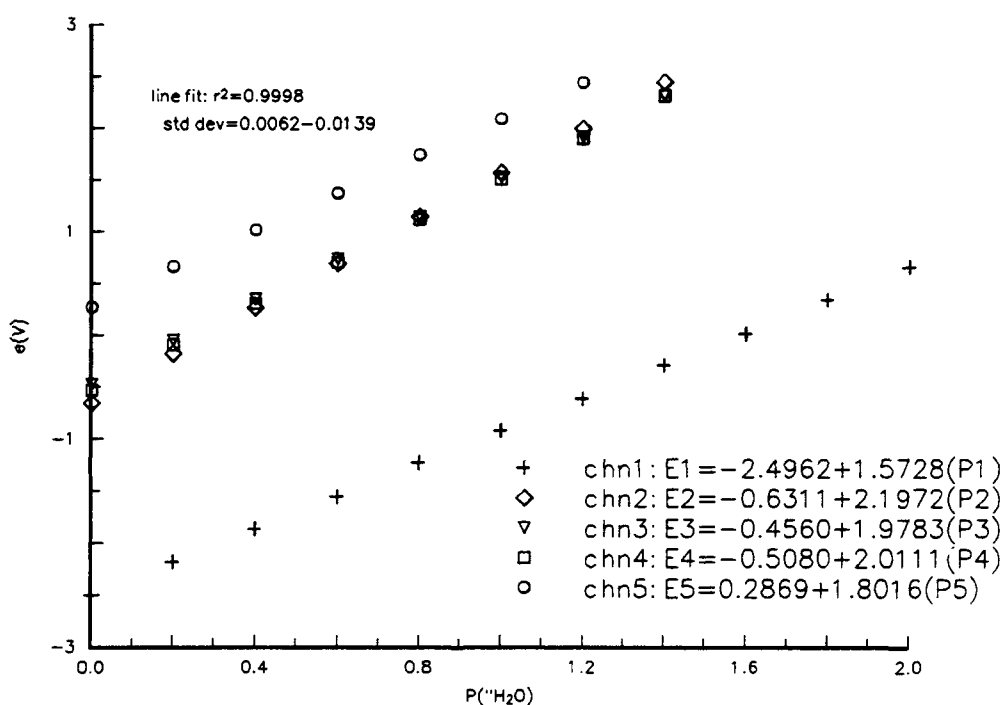
(b) January 1994

Figure 6: Sample five-channel pressure transducer calibration plots
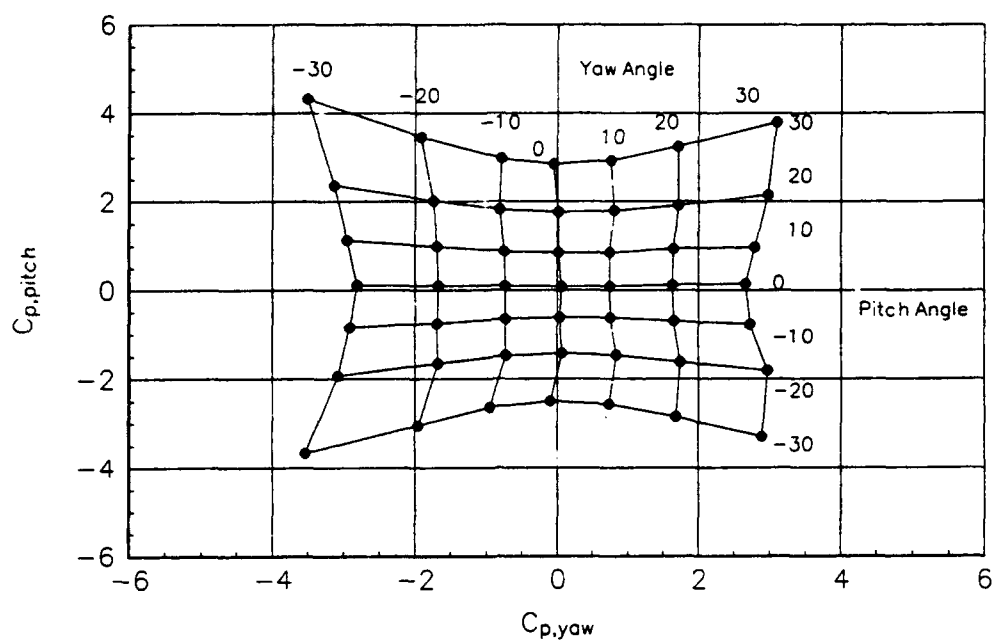
(a) $C_{p,yaw}$ vs. $C_{p,pitch}$
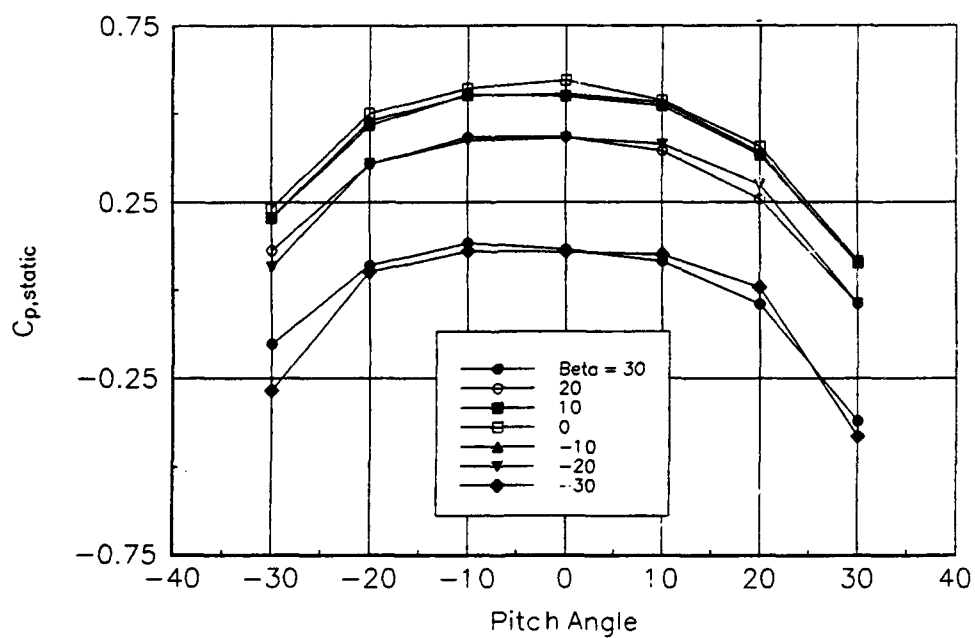
(b) $C_{p,static}$ vs. pitch angle

Figure 7: Five-hole probe calibration maps   (cont. on next page)
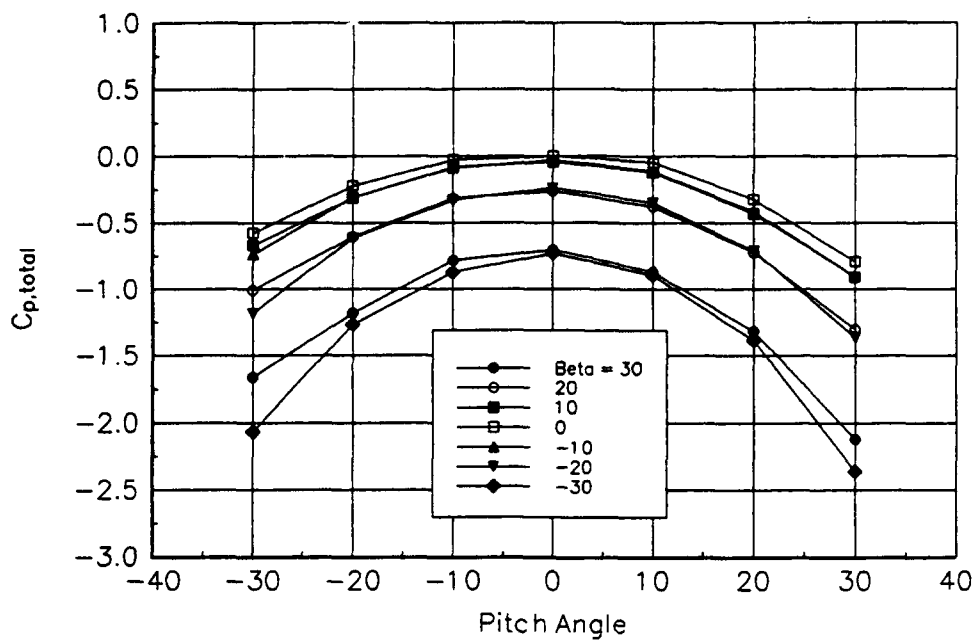
(c) $C_{p,total}$ vs. pitch angle

Figure 7: (cont.)

$$C_{p,total} = \frac{P_1 - P_T}{P_1 - P}$$ (3.4)

$$C_{p,static} = \frac{P - P_s}{P_1 - P}$$ (3.5)

The three velocity components were found using the measured pressure for each probe channel and interpolation of the preceding graphs. A computer code written by Prof. Camci and previous graduate students was used for data reduction. All five measured pressures were with respect to a common fixed reference (P_s). These pressures were used to compute $C_{p,yaw}$ and $C_{p,pitch}$ according to Equations 3.1, 3.2, and 3.3. Linear interpolation was then used with Figure 7(a) to find pitch and yaw angles. These angles were used with Figures 7(b) and 7(c) to find the total and static pressure coefficients. The total and static pressures were found by solving Equations 3.4 and 3.5. The mean velocity magnitude was determined using the inviscid approximation in Equation 3.6.

$$P_s + \frac{1}{2}\rho Q^2 = P_T$$ (3.6)

The three velocity components were found using the reference coordinate system depicted in Figure 5 and the known velocity magnitude and direction.

$$U = Q \cdot \cos\beta \cdot \cos\alpha$$ (3.7)

$$V = Q \cdot \sin\beta$$ (3.8)

$$W = Q \cdot \cos\beta \cdot \sin\alpha$$ (3.9)

Sources of error in the five-hole probe measurements and corresponding uncertainty analysis are discussed in detail in the Appendix.

An inviscid approximation is used to obtain all components of vorticity using the measurements taken in a single plane. The Euler equation for steady, incompressible, inviscid flow can be expressed as

$$\frac{1}{\rho}\vec{\nabla} P_t = \vec{V} \times \vec{\Omega}$$ (3.10)

neglecting body forces. The transverse components of total vorticity require streamwise gradients that are not measured in a single plane. The transverse vorticity components are approximated by using measured quantities and Equations 3.11 and 3.12.

$$\omega_y = \frac{1}{U}\left(\frac{1}{\rho}\frac{\partial P_t}{\partial Z} + V\,\omega_x\right) \qquad\qquad (3.11)$$
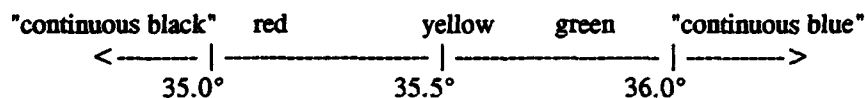
$$\omega_z = \frac{1}{U}\left(-\frac{1}{\rho}\frac{\partial P_t}{\partial Y} + W\,\omega_x\right) \qquad\qquad (3.12)$$

A central difference scheme is used to determine the required gradients from the measured values in the Y-Z plane. This technique has been used previously by Gregory-Smith et al. (1988) and Wiedner and Camci (1993b).

3.4. Heat Transfer Measurements

3.4.1. Liquid Crystal Background and Description

The physical properties of liquid crystals have been studied and known for over one hundred years, but have only come into practical scientific use over the past 20-30 years (Fergason, 1968 and Cooper et al., 1975). Liquid crystals are organic compounds and are useful because of their unique properties. They behave mechanically as liquids with very high viscosity, but optically they behave as crystals. Liquid crystals display different colors due to the scattering of light within the crystal-like structure and are used to register minute fluctuations in temperature, mechanical stress, electromagnetic radiation, and chemical environment. There are three major types of liquid crystals based on their structure and optical properties: smectic, nematic, and cholesteric. The crystals used in this study are a particular structure of the nematic type called chiral-nematic. The chiral-nematic and cholesteric liquid crystals possess an additional property that makes them especially useful for heat transfer studies. These liquid crystals "pass through the color band", that is, display different colors of visible wavelength from red to blue, as they are heated or cooled through a specific temperature range. The temperature dependence of a liquid crystal is a complex function of its molecular structure. Liquid crystals are available that display color bands anywhere from -40° to 285° C in bands of 1°-10° C. The liquid crystals in this study start displaying a red color at approximately 35° C and display the entire color band for a 1° C change in temperature as depicted below for an example continuous color spectrum.

```
"continuous black"   red          yellow      green    "continuous blue"
      <——— | —————————— | ————————— | ———>
             35.0°                 35.5°            36.0°
```

The liquid crystals exhibit the same color at the exact same temperature and the rate of change from color to color remains the same. The liquid crystals in this study were obtained in a water-based slurry and then air-brush deposited over black paint. The black paint ensures that any light not scattered by the crystals is absorbed by the paint. The physical properties that allow the reproducible temperature versus color

relationship degrade over time. For that reason, the liquid crystals used in this study were micro-encapsulated with gelatin in a polyvinyl alcohol binder to maintain their properties for over a year (Camci et al., 1992).

3.4.2 Experimental Method and Calibration

A hue capturing technique based on liquid crystal thermography, detailed in Camci et al. (1992), is used to measure the endwall surface temperature. A high sensitivity video camera is used to take images of the liquid crystal color band on the endwall after steady-state conditions are reached. The images are stored on magnetic tape and processed based on hue, saturation, and intensity discrimination. The Data Translation (DT) 2871 (HSI) Color Frame Grabber is a computer plug-in circuit board that captures color images from standard color video sources for image processing. Image processing includes frame averaging, filtering, storage, and display. The color images are captured and displayed in real time at a rate of 30 frames per second. Standard color video sources refer to color video cameras (VCRs) using National Television Systems Committee (NTSC) storage and transmission standards. The NTSC signal from the video camera, a Sony Model CCD-V9/V90, is decoded from a red, green, blue (RGB) output format using a DT 2869 Video Encoder/Decoder circuit board for input to the color frame grabber, DT 2871. The RGB video signals representing the color image are converted to new values representing hue, saturation, and intensity (HSI) data. The DT 2871's 10 MHz RGB→HSI converter receives 8-bit red, 8-bit green, and 8-bit blue pixel values from three analog-to-digital (A/D) converters and outputs 8-bit hue, 8-bit saturation, and 8-bit intensity values to three onboard frame buffers for storage. The RGB→HSI conversion is calculated in real time. The color image in storage is a combination of four frame buffers. One frame buffer each for hue, saturation, and intensity and the fourth buffer for text or graphic overlay information. The overlay buffer can be superimposed on the output color image. Each buffer is 256 Kbyte arranged as 512 x 512 x 8-bit. Thus, the color frame grabber hardware can accommodate a 512 x 512 pixel representation of the screen.

The HSI image format approximates the way humans perceive and interpret color better than the RGB format (Camci et al., 1992). Hue, saturation, and intensity are relatively independent attributes that completely describe a color. The RGB format, on the other hand, is highly cross-correlated. The RGB buffers must be viewed together to get meaningful information, whereas a hue buffer (or saturation or intensity) can stand alone to yield useful information about the image as it does in this study. Hue is the color attribute describing a pure color. Saturation describes the degree of dilution of the pure color with white. Intensity describes the relative brightness or darkness in an image.

The calibration of the liquid crystals is the process of determining the precise relationship between the hue value of the liquid crystal and its temperature. Two k-type, thin-film thermocouples were calibrated against a mercury thermometer before being adhered to the duct endwall as described in section 3.1. The liquid crystals are calibrated against the thermocouples by passing the color band across the thermocouple

several times by varying the voltage drop across the endwall bus bars and recording the entire event on video tape. Spatial averaging is used in the calibration computer code to use the hue values of the nine pixels surrounding the thermocouple location to determine the average hue value assigned to the temperature of the thermocouple at that time. Temporal averaging is incorporated by using the values of 30 separate image frames obtained over several seconds of elapsed time. This spatially and temporally averaged calibration process was completed three times at two separate locations on the endwall and a linear hue versus temperature relationship was found for each location, Figure 8.

The camera captures images at 30 frames per second and each frame is discretized as 512 x 480 pixels when viewed on the computer screen. The liquid crystal color band (from red to dark blue) occupied between 10 and 50 pixels depending on the magnitude of the temperature gradient. In order to gain the temperature for the entire endwall surface the color band region was moved from area to area by changing the voltage drop across the bus bars. This does not affect the measured heat transfer coefficient since h is independent of thermal boundary conditions in the temperature region of the present study. Each fence configuration used in the heat transfer study required 23-29 separate images to map the entire endwall surface. Each of those images corresponded to a distinct voltage drop across the bus bars and was the averaged result of five separate frames captured at the same conditions. Freestream temperature was measured using a fine wire, K-type thermocouple probe. This probe was calibrated against the same mercury thermometer as the thermocouples.

The heat transfer to the endwall surface was determined for steady state conditions using the liquid crystals and thin-foil resistive heating. A complete description of the technique is given in Wiedner and Camci (1993a). The convective heat transfer coefficient on the endwall surface was determined using Equation 3.13.

$$h = \frac{\dot{q}_{conv}}{(T_w - T_\infty)} = \frac{\dot{q}_{gen} - \dot{q}_{cond} - \dot{q}_{rad}}{(T_w - T_\infty)} \qquad (W/m^2 \, K) \qquad (3.13)$$

A finite element numerical code discussed in Camci (1989) was used to determine the non-uniform heat flux generated in the thin foil. The code determines voltage potential distribution in the foil, $V(x,y)$, by solving the electrostatic boundary value problem governed by the Laplace equation expressed in Equation 3.14.
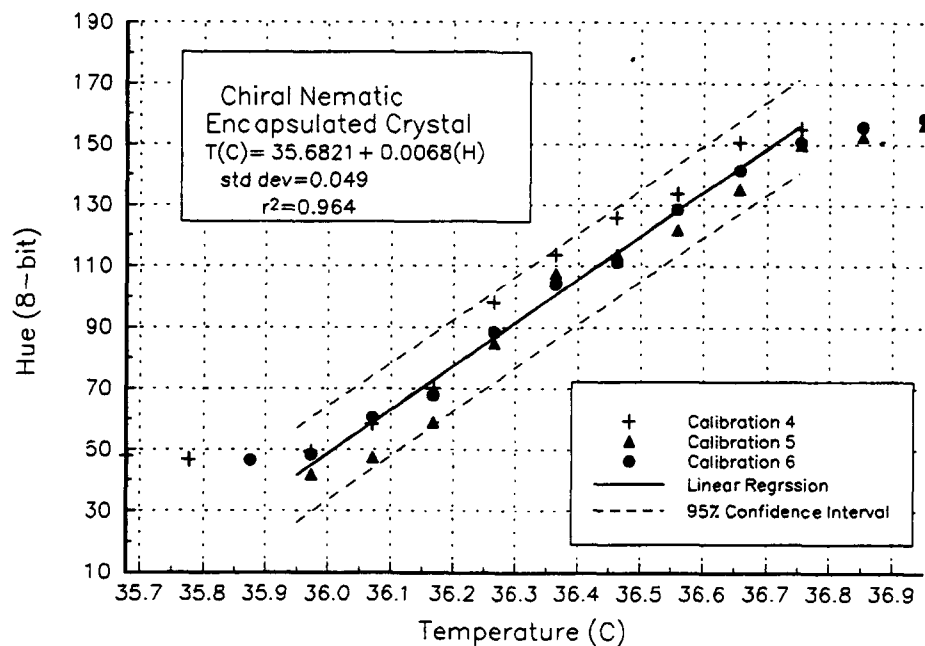
$$\vec{\nabla}^2 V(x,y) = 0 \qquad (3.14)$$

The boundary conditions are:

      a. uniform potential at the bus bar and foil junctions.

      b. zero current flux normal to the unbounded streamwise edges.

The electric field, E (V/m), and current density, J (A/m^2), are determined from the calculated voltage
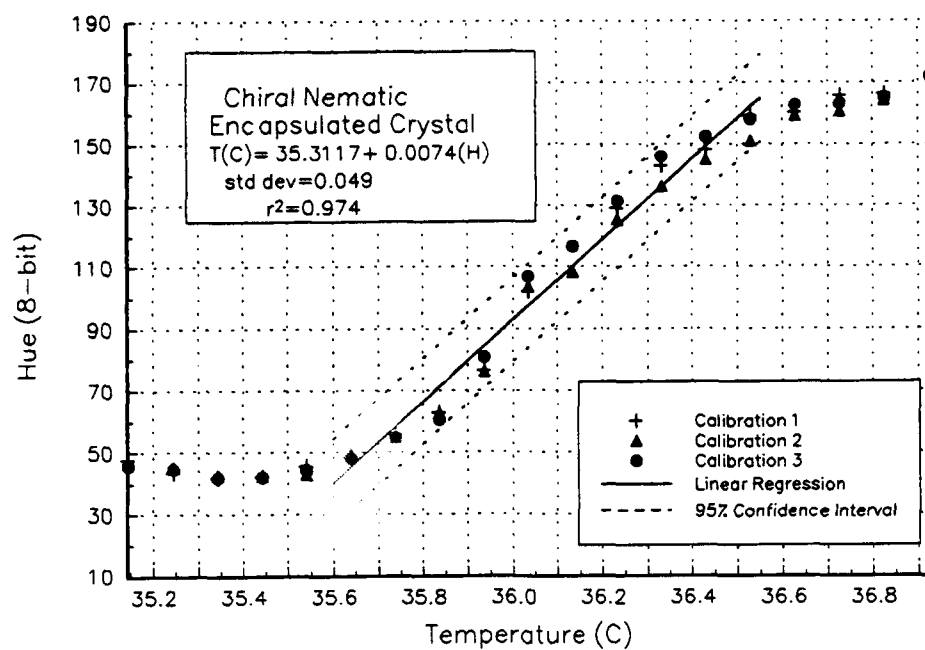
(a) Calibration using thermocouple located at 67°

(b) Calibration using thermocouple located at 28°

Figure 8: Liquid crystal calibration, hue vs. temperature relationship

potential distribution using Equations 3.15 and 3.16.

$$\vec{E} = -\vec{\nabla}V \qquad (V/m) \qquad (3.15)$$

$$\vec{J} = \sigma\vec{E} \qquad (A/m^2) \qquad (3.16)$$

where σ is the foil conductivity $((ohm \cdot m)^{-1})$. The generated surface heat flux is determined using Equation 3.17.

$$\dot{q}_{gen} = \delta\vec{E} \cdot \vec{J} \qquad (W/m^2) \qquad (3.17)$$

where δ is the foil thickness (m).

Conduction from the foil to the endwall was estimated using one-dimensional analysis. An infrared thermometer was used to determine the surface temperature of the ambient side of the heated endwall during each experimental run. The temperature measurements, T_a, were used to form a high density grid directly opposite the color band region on the frontside of the endwall where liquid crystals were used to determine the surface temperature, T_w. The heat flux lost to conduction was calculated using Equation 3.18.

$$\dot{q}_{cond} = \frac{k}{l}(T_a - T_w) \qquad (W/m^2 K) \qquad (3.18)$$

where k is the foil thermal conductivity (W/(m K)) and l is the foil thickness (m). The effects of lateral conduction along the edges of the heated endwall were discussed in Wiedner and Camci (1993a) and the maximum lateral conduction was less than .25 % of the generated heat flux. Conduction heat flux through the endwall was typically 5-8% of the generated heat flux at any point. Radiation losses were estimated using assumptions of black-body emissivity and thermal equilibrium between the free-stream air and unheated duct surfaces. Shape factors for the radiation heat flux from the heated endwall to adjacent and opposite duct surfaces and from incandescent lamps to the heated endwall were estimated using two-dimensional analysis. Total radiation heat flux was typically 6-9% of the local generated heat flux.

Heat transfer measurements were made for two different fence configurations: one thick fence (4.7 mm wide, full-length, half-height) and the thin fence (1.0 mm wide, full-length, half-height). These were compared with the endwall heat transfer for the no-fence duct presented in Wiedner and Camci (1993b).

Chapter 4
EXPERIMENTAL RESULTS AND DISCUSSION

4.1. Overall Flow Field and Aerodynamic Losses

The inlet boundary layer profile and turbulence intensity measured at a distance of 2.75 duct widths upstream of 0° on the endwall is shown in Figure 9. Measurement of the entire inlet plane revealed relatively uniform boundary layer thicknesses on all surfaces, Figure 10. Characteristics of the inlet boundary layer as reported in Wiedner and Camci (1993b) are: δ_{99}=25.4 mm, displacement thickness = 4.6 mm, momentum thickness = 2.6 mm, and shape factor = 1.8. Turbulence intensity ranges from .7% in the freestream to 6.8% at the edge of the measurement grid, Z/D=.975.

Figures 11-13 show the velocity and total pressure fields measured at the 90° plane (Y-Z) for all fence cases. All values are nondimensionalized with the inlet centerline velocity and dynamic pressure. Figure 11 shows the trade-off between an additional momentum deficit due to the fence and the modification to the flowfield near the suction surface. The action of the passage vortex sweeping low momentum fluid from the duct boundary layers onto the suction surface is interrupted to varying degree by each fence case. The additional low momentum fluid from the boundary layers on the fence surfaces varies according to fence height and length. The longer fences influence streamwise velocity over a greater region of the duct than the shorter fences. The alteration in the streamwise velocity field requires quantitative measurement to determine if the tradeoff is an overall positive or negative effect. Total pressure loss in Figure 12 shows the same trends as the momentum deficit. Viscous losses in the boundary layer are seen as total pressure losses that are concentrated in the passage vortex interaction region near the duct centerline on the suction surface in the no-fence case. The cumulative effect is the high-loss core seen in Figure 12(f). The fence reduces the high loss core by forcing the passage vortex into the freestream flow where it is convected downstream further before it can combine with the high loss fluid from the opposite endwall. This is depicted graphically in Figure 12 by the distortion and translation of the characteristic "mushroom" shape of the high-loss core on the suction surface. All fence cases distort the high-loss core to some degree. The shortest and lowest fence, Figure 12(d), has the least impact. The longest and highest fence has the greatest impact on the high-loss core. The high-loss core is visibly pushed against the suction surface on the fence side and the center has moved from Z/D=.51 (for the no-fence case) to Z/D=.58 in Figure 12(a). A net increase or decrease of loss in any of the fence cases is not clear. To have an overall positive effect the fence must not just redistribute the boundary layer fluid, it must reduce loss mechanisms such as viscous effects in mixing or other entropy loss. The fence has prevented (or disturbed) the movement of all the boundary layer fluid by the passage vortex into the high-loss core. Figure 12 can be used quantitatively to show the trade-off between additional fence losses and reduced passage vortex losses. The total pressure
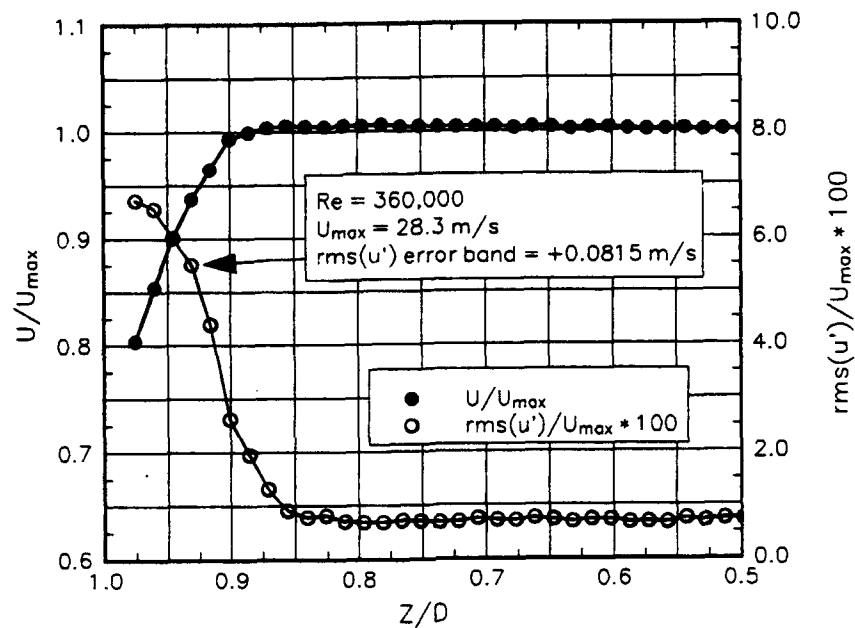
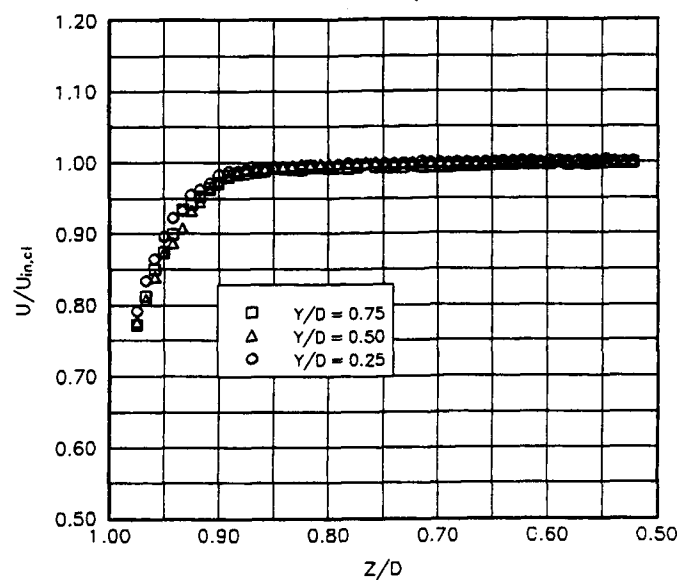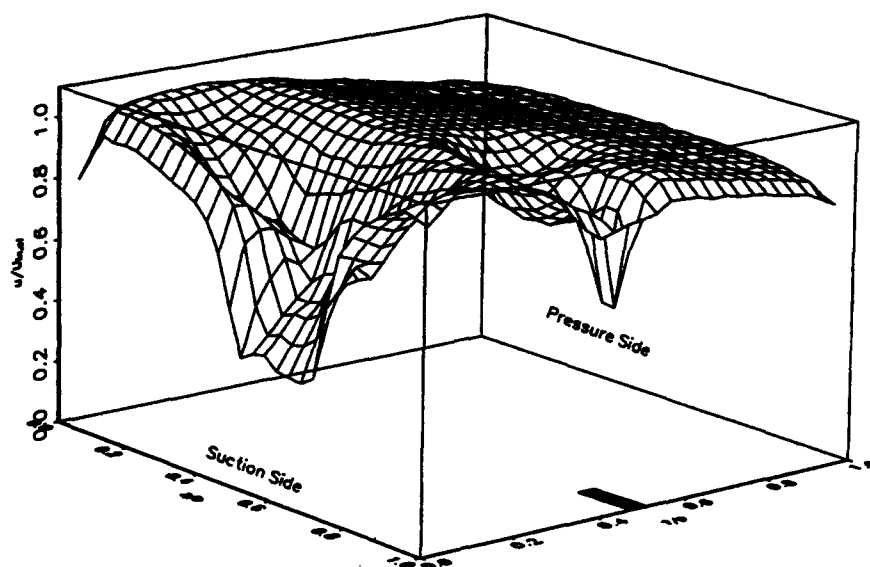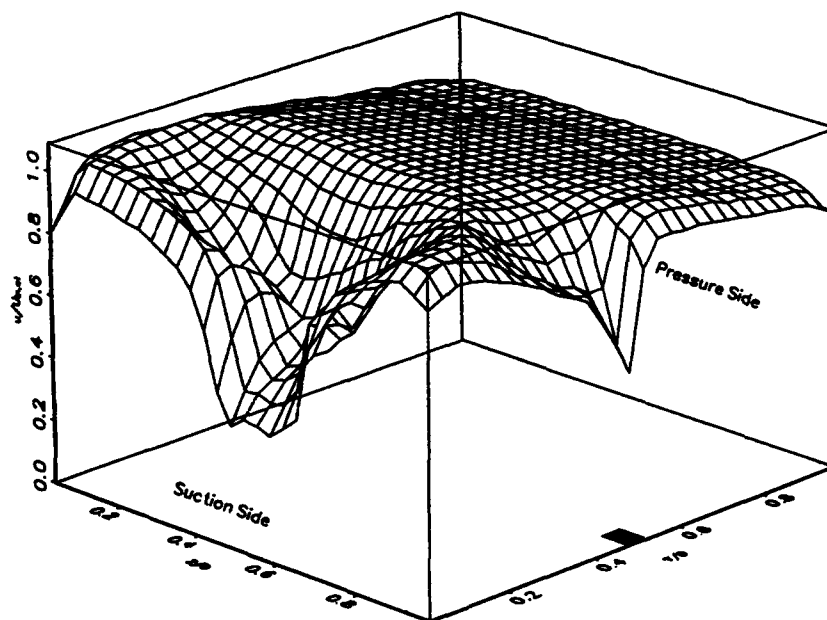Figure 9: Endwall boundary layer profile and turbulence intensity at the duct inlet

Figure 10: Endwall boundary layer velocity profiles at the duct inlet
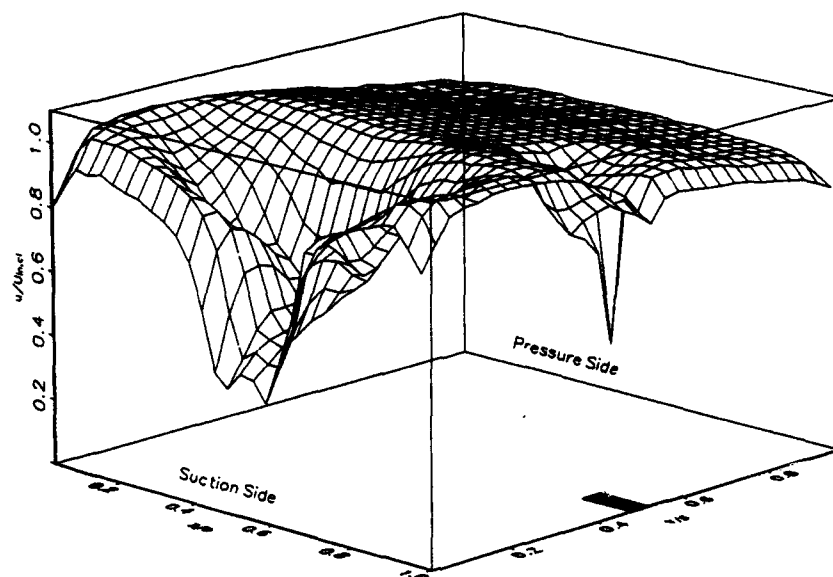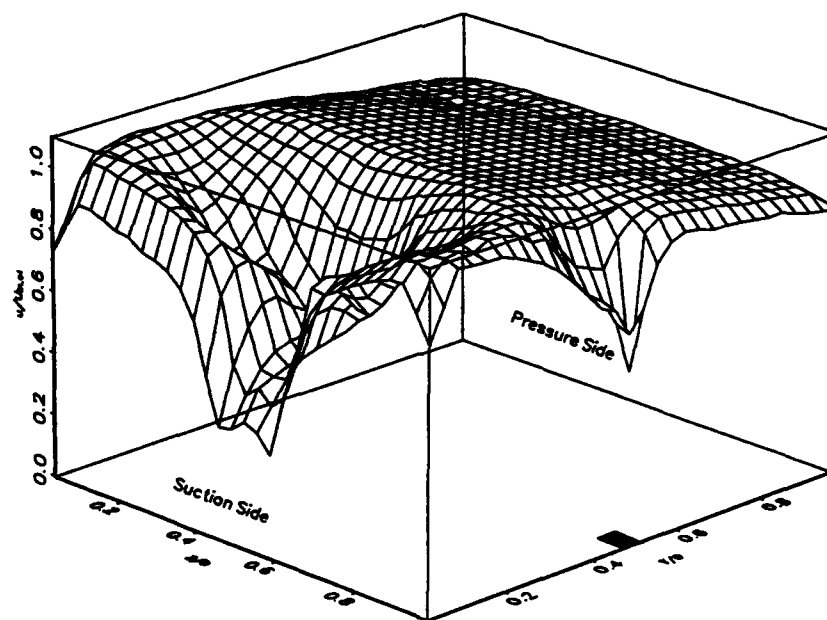
(a) 4.7 mm wide, full-length, full-height fence

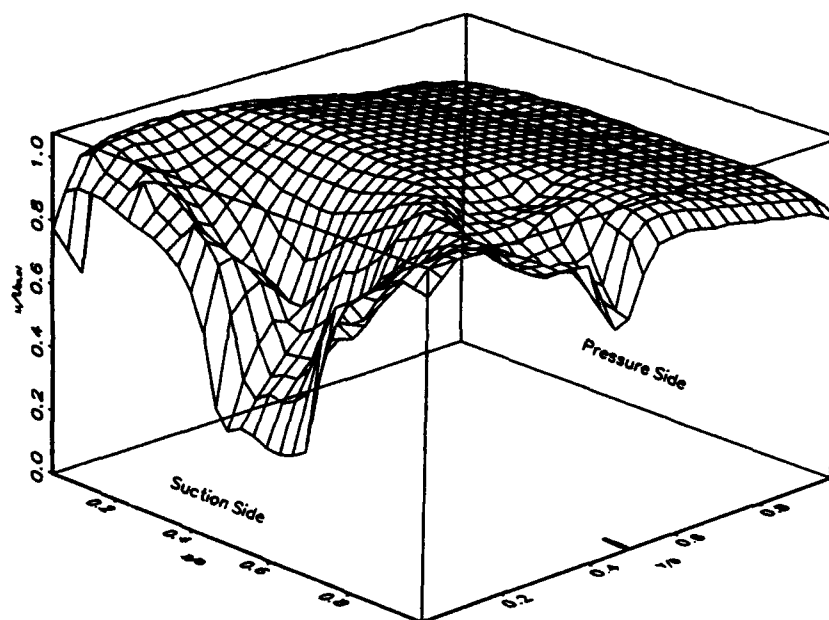(b) 4.7 mm wide, full-length, half-height fence

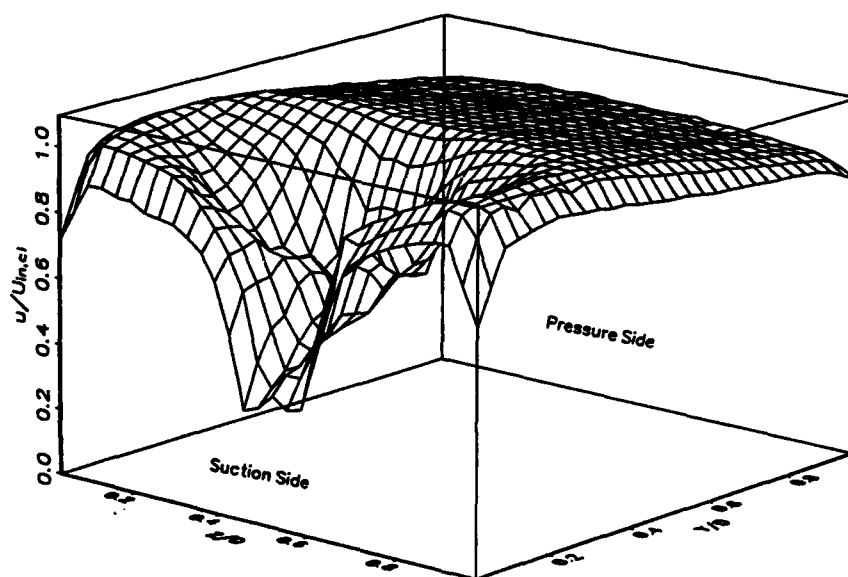Figure 11: Mean streamwise velocity surface contours, $U/U_{in,cl}$, 90° plane   (cont. on next page)

(c) 4.7 mm wide, half-length, full-height fence

(d) 4.7 mm wide, half-length, half-height fence
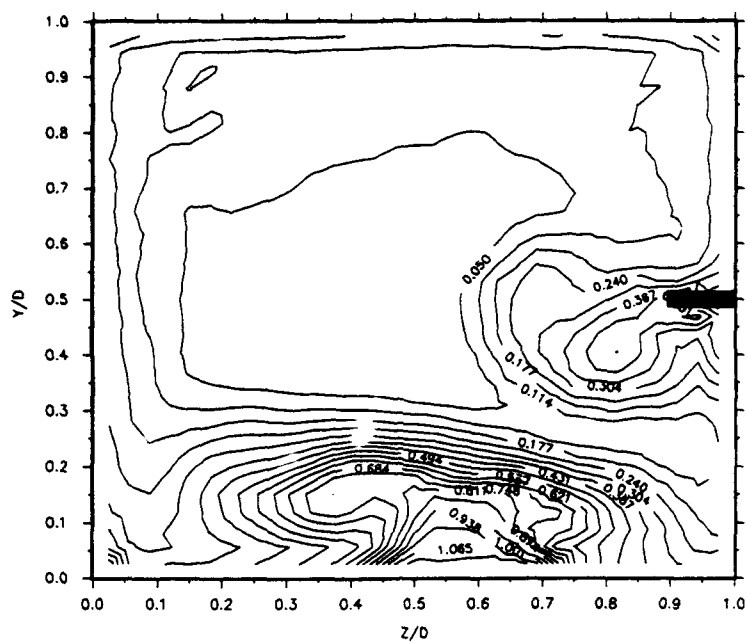
Figure 11: (cont.)

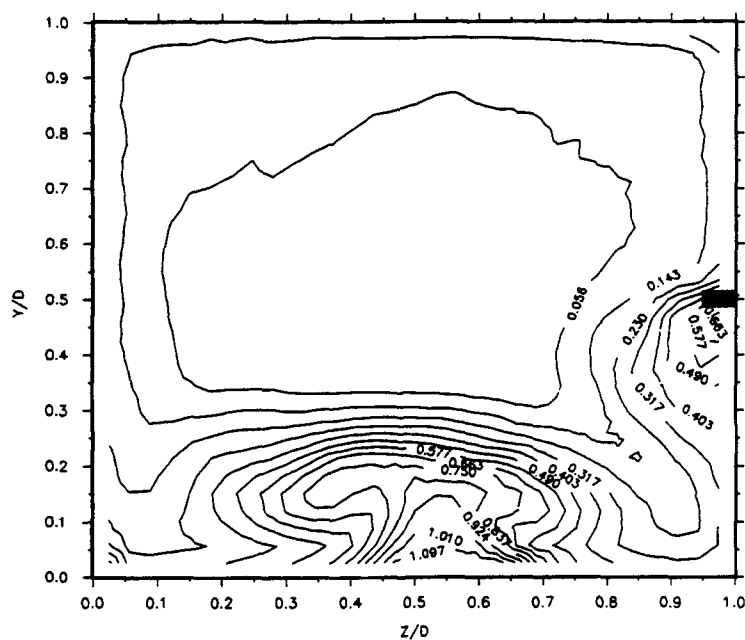(e) 1.0 mm wide, full-length, half-height fence

(f) no fence

Figure 11: (cont.)

(a) 4.7 mm wide, full-length, full-height fence
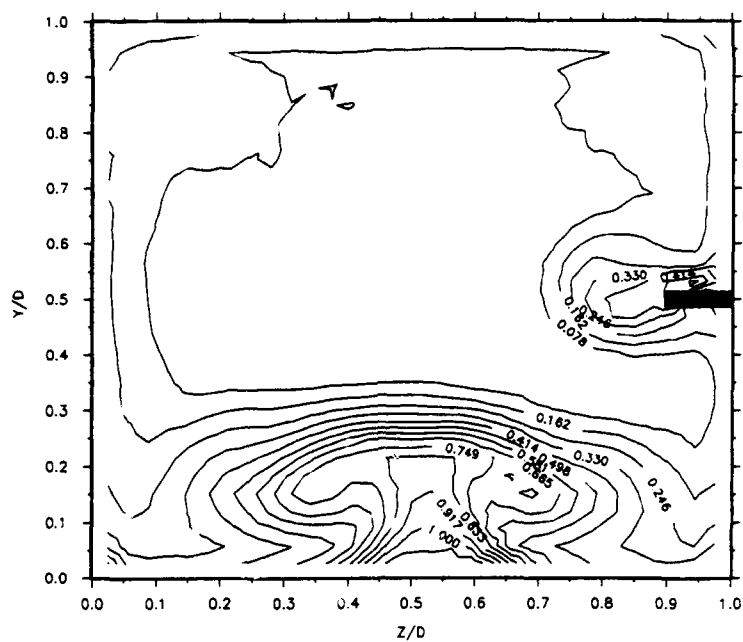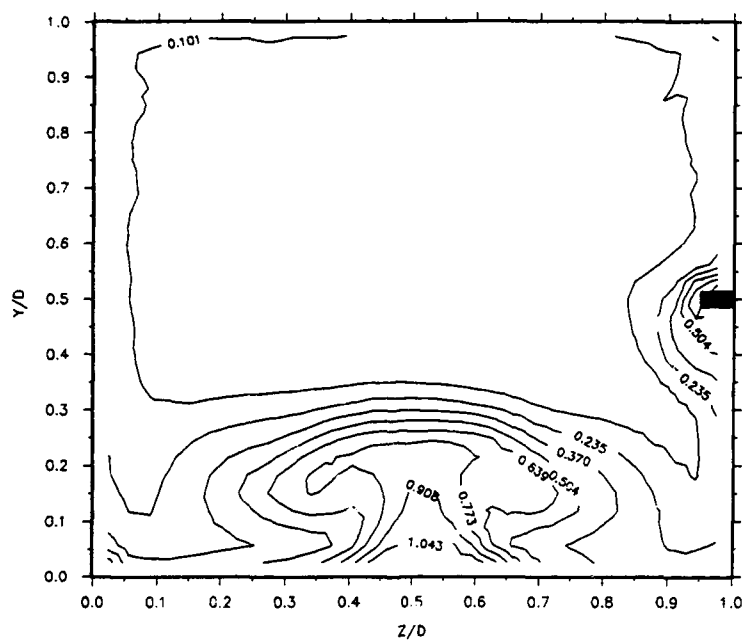

(b) 4.7 mm wide, full-length, half-height fence

Figure 12: Total pressure coefficient, $(P_{t,in,cl}-P_t)/.5\rho U^2_{in,cl}$, 90° plane   (cont. on next page)
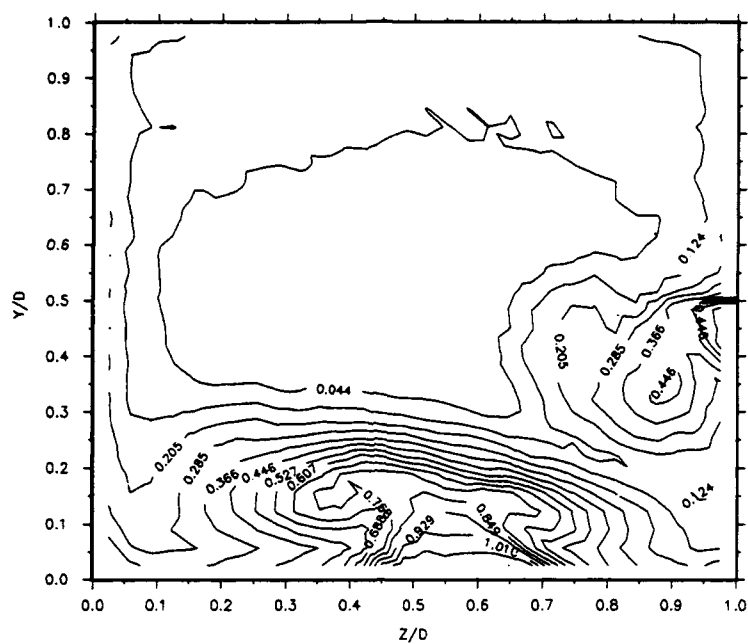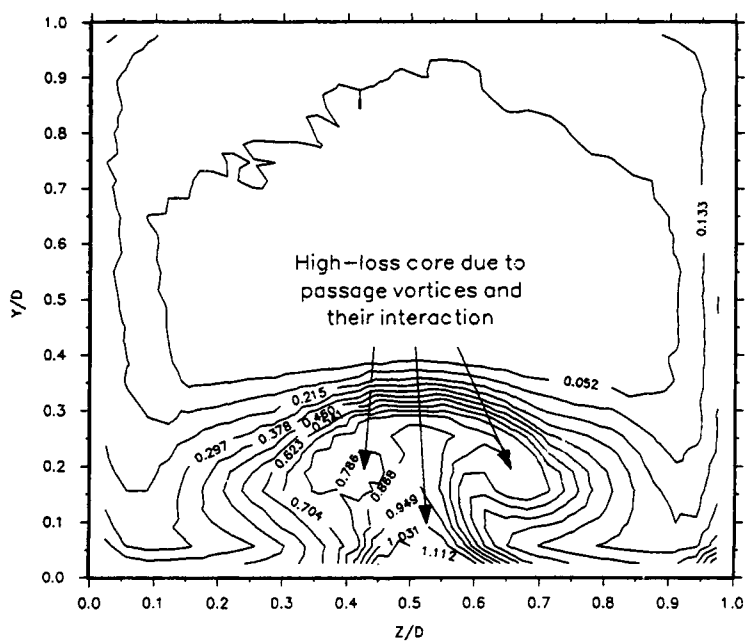
(c) 4.7 mm wide, half-length, full-height fence

(d) 4.7 mm wide, half-length, half-height fence

Figure 12: (cont.)

29

(e) 1.0 mm wide, full-length, half-height fence

(f) no fence

Figure 12: (cont.)

coefficient, streamwise velocity, and secondary flow velocity for all fence cases are passage averaged at the 90° plane and presented in Table 1. Both full-height fences add to the overall total pressure loss compared to the no-fence case. All three half-height cases (two thick fences and one thin) reduce the total pressure loss in the duct in agreement with the findings of Kawai et al. (1989) for a cascade. The half-length, half-height fence of case (d) reduces total pressure loss even greater than the thin, full-length fence of case (e). This is evidence that there is an optimum fence length as well as a critical fence height for reducing total pressure loss. The passage vortex is still relatively weak at 45°, as shown in Wiedner and Camci (1993b), and Figure 12(d) shows that a half-length fence is long enough to reduce the passage vortex without adding excessive viscous loss.

TABLE 1: Comparison of aerodynamic characteristics at 90° plane for all fence cases

Fence configuration	$\bar{C}_{pt}$	%ch	$\overline{U/U}_{in,cl}$	%ch	$\overline{\sqrt{(V^2+W^2)}/U}_{in,cl}$	%ch
(a) 4.7mm wide,full-length,full-height	.182	+8.9	.915	-.3	.139	+13.9
(b) 4.7mm wide,full-length,half-height	.165	-1.2	.918	0	.135	+10.7
(c) 4.7mm wide,half-length,full-height	.173	+3.6	.910	-.9	.140	+14.8
(d) 4.7mm wide,half-length,half-height	.156	-6.5	.925	+.9	.125	+ 2.5
(e) 1.0mm wide,full-length,half-height	.159	-4.8	.918	0	.129	+ 5.7
(f) no fence	.167		.918		.122	

Notes: 1. %ch = percentage change from no-fence case
         2. increased exit velocity due to fence blockage (decreased area) is ≤ .3%

Figure 13 is a graphical depiction of where the change in pressure loss occurs across the 90° plane between each fence case and the no-fence case. The comparison is made at each point and the "zero" plane represents the total pressure loss for the no fence case. Thus, areas below the zero plane represent reduced total pressure loss due to a weaker passage vortex on the fence side and areas above the zero plane represent increased pressure loss due to the fence. Figure 13 offers the best representation of the total pressure loss reduction and enhancement mechanisms in the duct with the endwall fence. The original losses in the duct due to the passage vortices are reduced significantly by the full-length fences. However, these gains are diminished by the losses generated from the fences.
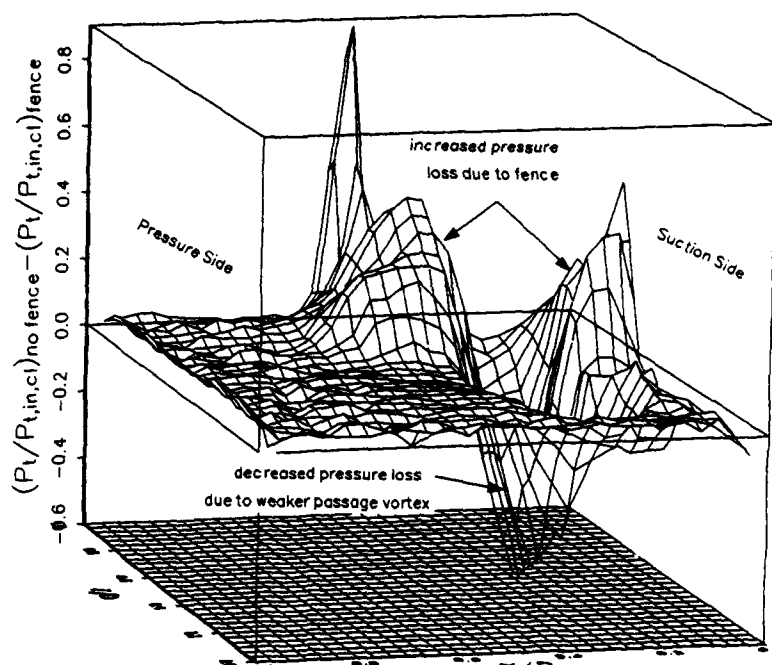
(a) 4.7 mm wide, full-length, full-height fence
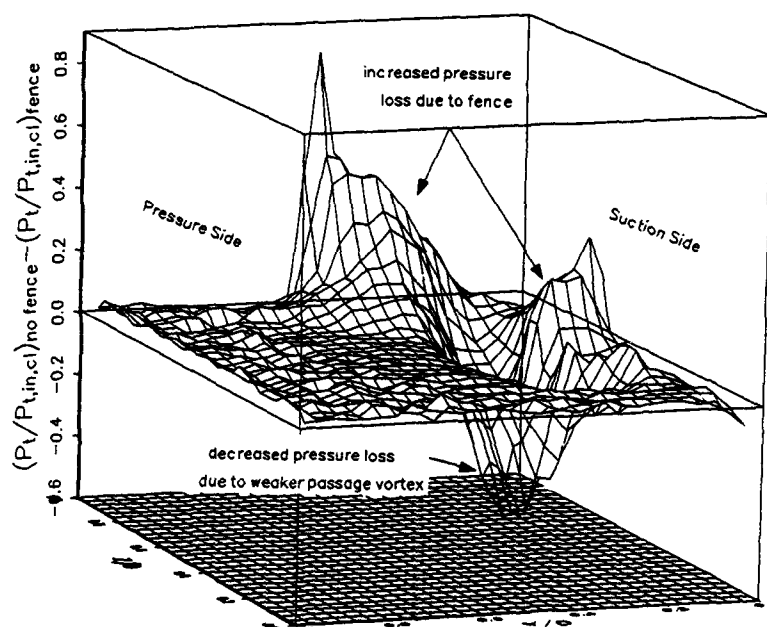
(b) 4.7 mm wide, full-length, half-height fence

Figure 13: Total pressure comparison with no-fence case (point to point), $(P_t-P_{t,in,cl})_{no\ fence}-(P_t-P_{t,in,cl})_{fence}$, 90° plane   (cont. on next page)
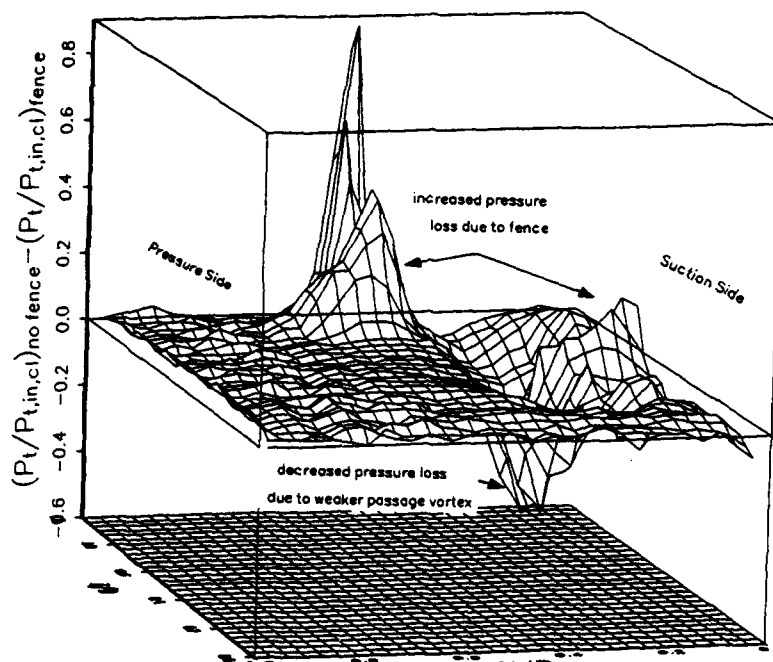
(c) 4.7 mm wide, half-length, full-height fence

(d) 4.7 mm wide, half-length, half-height fence

Figure 13: (cont.)

(e) 1.0 mm wide, full-length, half-height fence

Figure 13: (cont.)

4.2. Secondary Flow Field

The fence effects the magnitude and direction of secondary flow along the endwall dramatically. Figure 14 clearly shows the change in secondary flow vector magnitude, $\sqrt{(V^2+W^2)}$, along the fence endwall and the fence side of the duct, $Z/D \geq .5$. Combining Figures 12 and 14 shows that the fence cases with the highest amounts of pressure loss near the endwall region between fence and suction surface, cases a, b, and e (all full-length cases), are also the fences with the lowest secondary flow along the endwall. This is evidence that the full-length fences interrupt the convection of high-loss fluid from the endwall boundary layer by the passage vortex and results in the build-up of that high-loss fluid along the endwall. Remember that fences in Figures 14(b) and 14(e) also reduce overall total pressure loss in the duct.

The passage averaged value of secondary velocity magnitude is shown in the last column of Table 1. Even cases (a), (b) and (e) that reduce secondary flow along the endwall result in overall increases of passage averaged secondary velocity magnitude in the duct. The complex nature of the fence effects on secondary flow is illustrated by the secondary flow velocity vectors shown in Figure 15. All fence cases have varying amounts of the endwall flow moving from suction toward pressure surface. This is opposite the normal direction. Local static pressure contours confirm the vector information (not shown). In addition, all fence cases have interaction of varying strength vortices on the fence endwall at $Y/D = .15-.35$. This is associated with endwall heat transfer effects discussed in a later section. The full-height cases, Figures 15(a) and 15(c), show the fence acting as a blade with two separate passage vortices developing along the endwall between pressure and suction surfaces on the fence and pressure and suction surfaces on the duct. The thick and thin half-height cases, Figures 15(b) and 15(e), develop a pair of counter rotating vortices between the fence and suction surface as if the fence were a sharp obstacle in the path of secondary flow along the endwall. Another half-height fence, Figure 15(d), shows the same pair of vortices, but not developed as far as the others since it is a half-length fence. The secondary flow for all the full-length fences is significantly reduced in the endwall/suction surface junction compared to the no-fence and half-length fence cases. All fence cases and the no-fence case display interaction of a passage vortex system on the endwall near the pressure surface at $Y/D = .90$. The contour of secondary kinetic energy is clear evidence that the full-length fences, Figures 16(a), 16(b), and 16(e), have reduced the strength of the passage vortex for $Z/D \geq .5$.

4.3. Vorticity Field

The vorticity field is investigated to gather any correlation between vortex action and heat transfer effects seen on the endwall. Mean streamwise vorticity magnitude and sign (in the right-handed sense) is shown in Figure 17. The negative streamwise vorticity between the fence and suction surface is noted for all fences. The effect of these vortices is not completely understood, though their collocation with regions of high total pressure loss is clear. This fluid movement is in contrast to the normal passage vortex of the
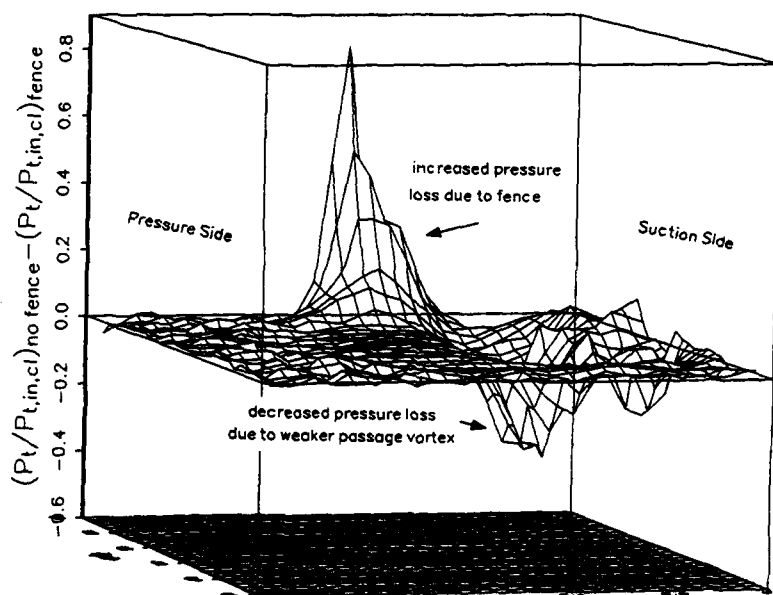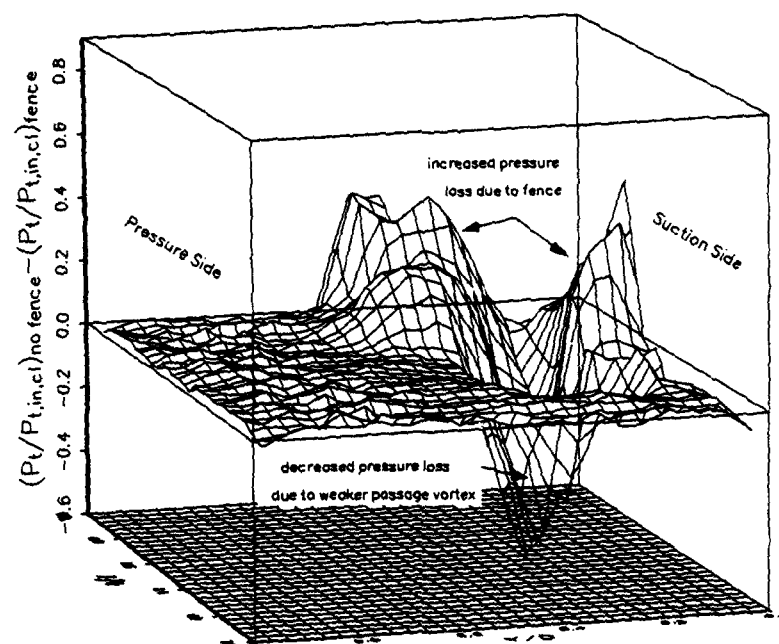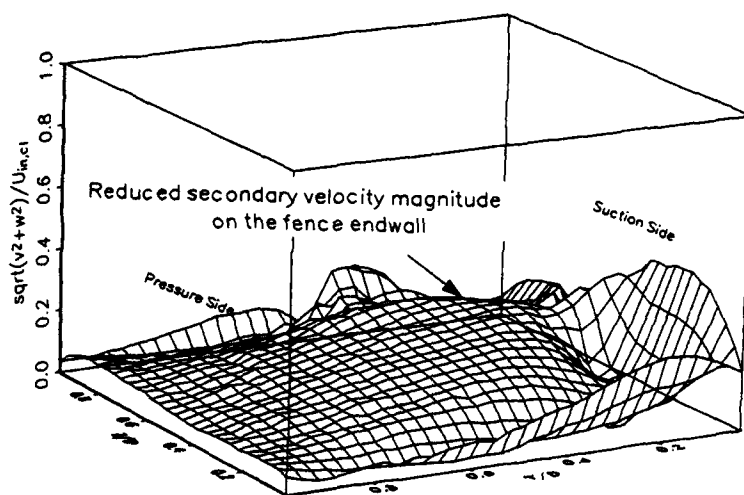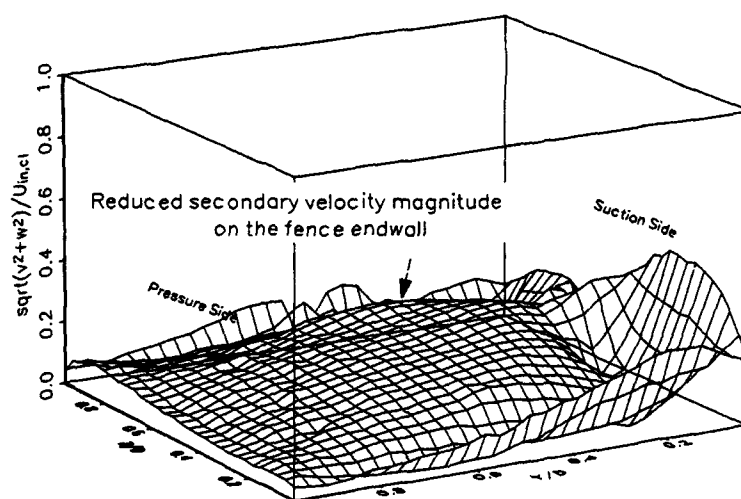
(a) 4.7 mm wide, full-length, full-height fence

(b) 4.7 mm wide, full-length, half-height fence

Figure 14: Mean secondary velocity surface contours, $\sqrt{(V^2+W^2)}/U_{in,cl}$, 90° plane (cont. on next page)
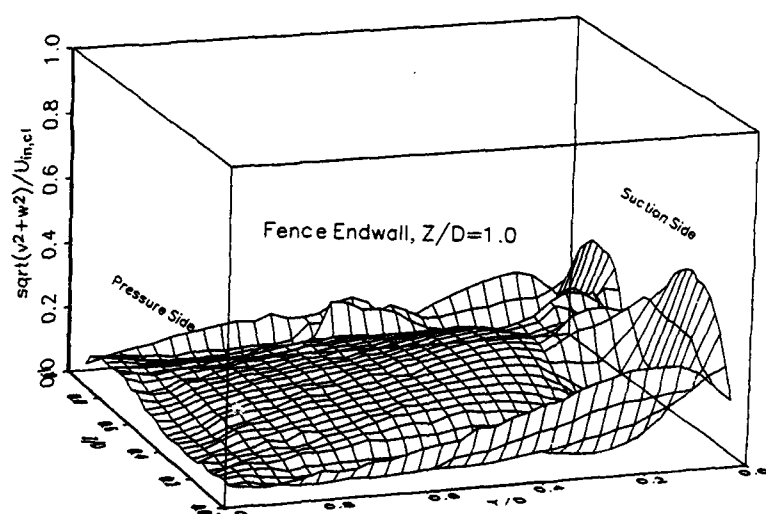
(c) 4.7 mm wide, half-length, full-height fence

(d) 4.7 mm wide, half-length, half-height fence
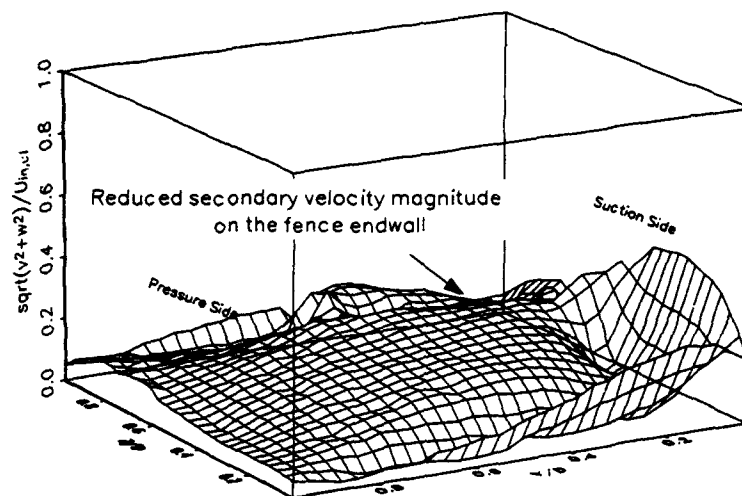
Figure 14: (cont.)

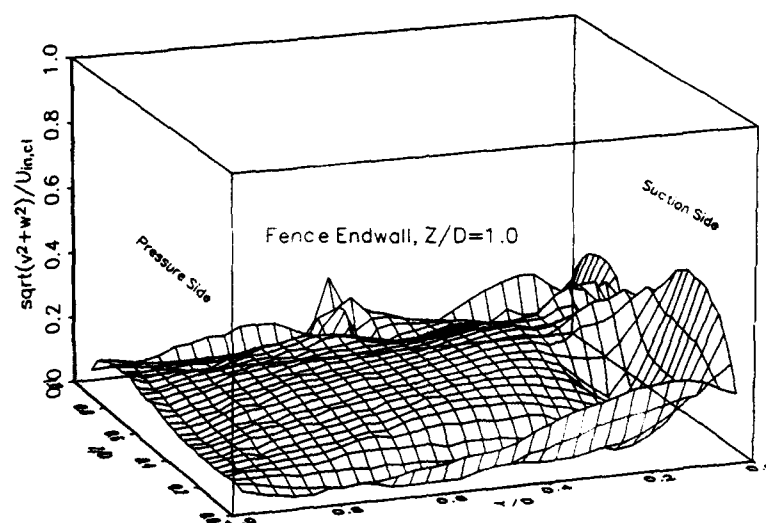(e) 1.0 mm wide, full-length, half-height fence

(f) no fence

Figure 14: (cont.)

(a) 4.7 mm wide, full-length, full-height fence

(b) 4.7 mm wide, full-length, half-height fence

Figure 15: Mean secondary velocity vectors, $\sqrt{(V^2+W^2)}$, 90° plane ($\rightarrow$ = 5 m/s)   (cont. on next page)
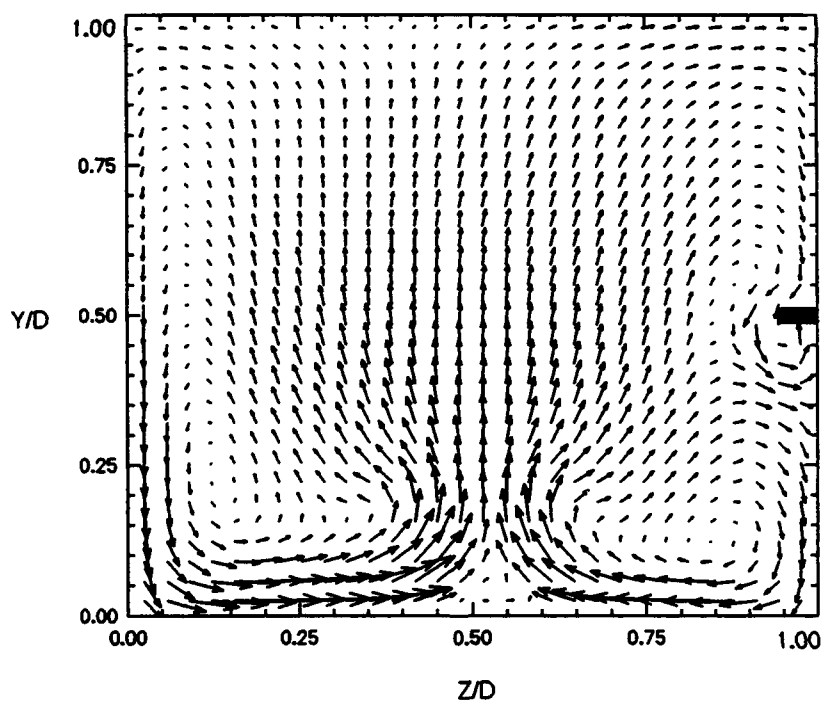
(c) 4.7 mm wide, half-length, full-height fence

(d) 4.7 mm wide, half-length, half-height fence
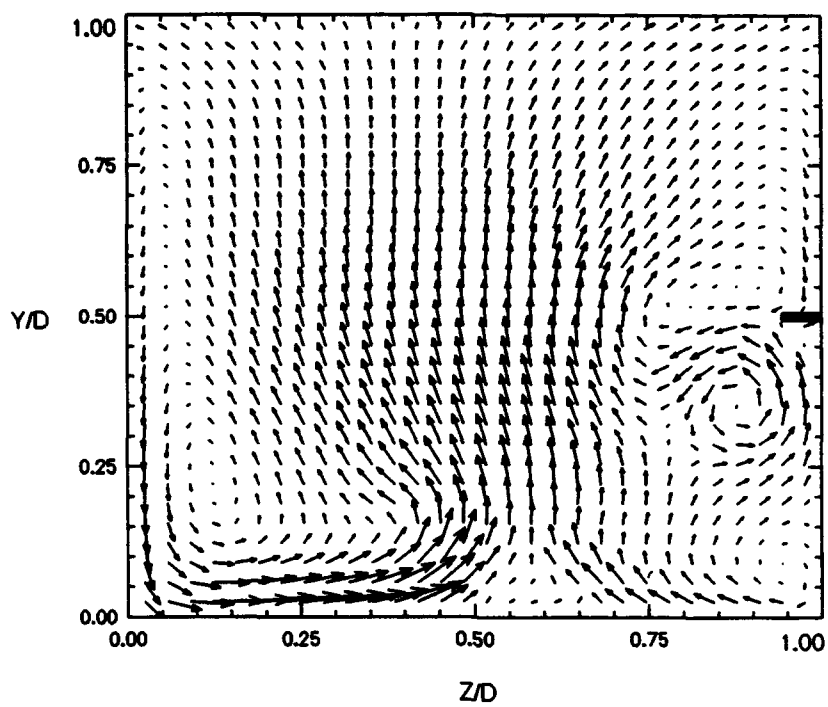
Figure 15: (cont.)

(e) 1.0 mm wide, full-length, half-height fence
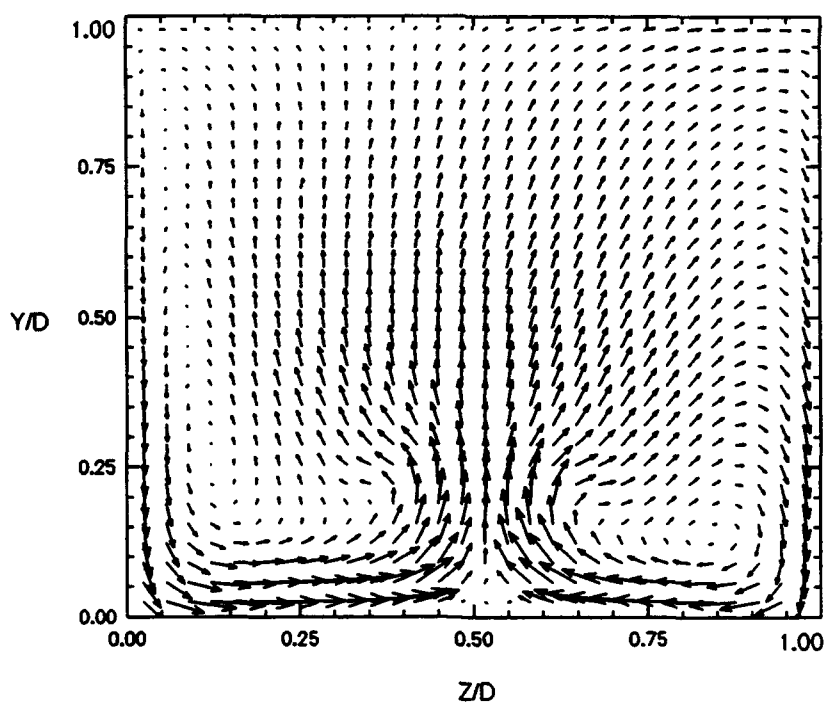
(f) no fence

Figure 15: (cont.)
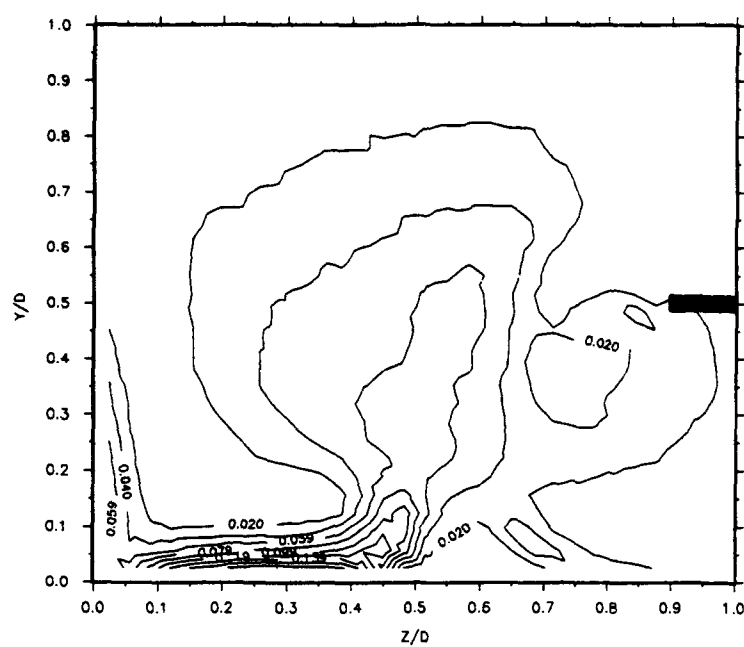
(a) 4.7 mm wide, full-length, full-height fence
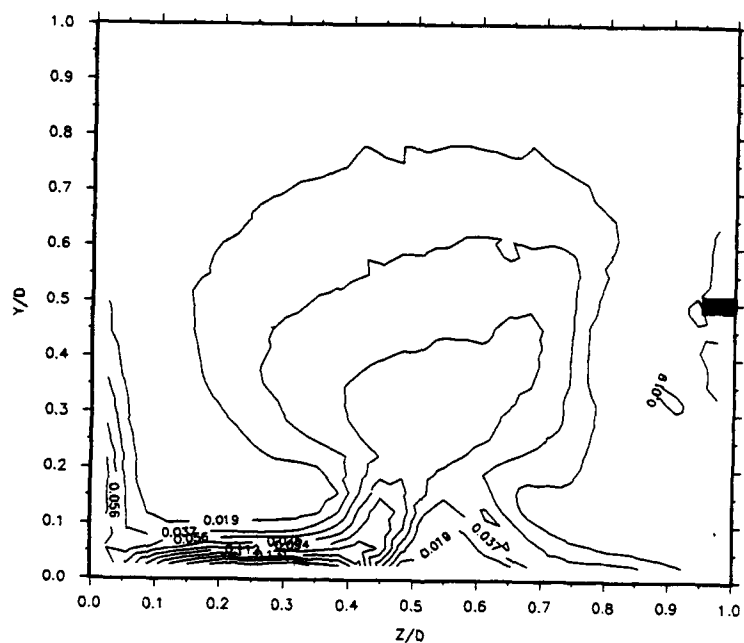
(b) 4.7 mm wide, full-length, half-height fence

Figure 16: Secondary kinetic energy, $(V^2 + W^2)/U^2_{in,cl}$, 90° plane

(c) 4.7 mm wide, half-length, full-height fence

(d) 4.7 mm wide, half-length, half-height fence
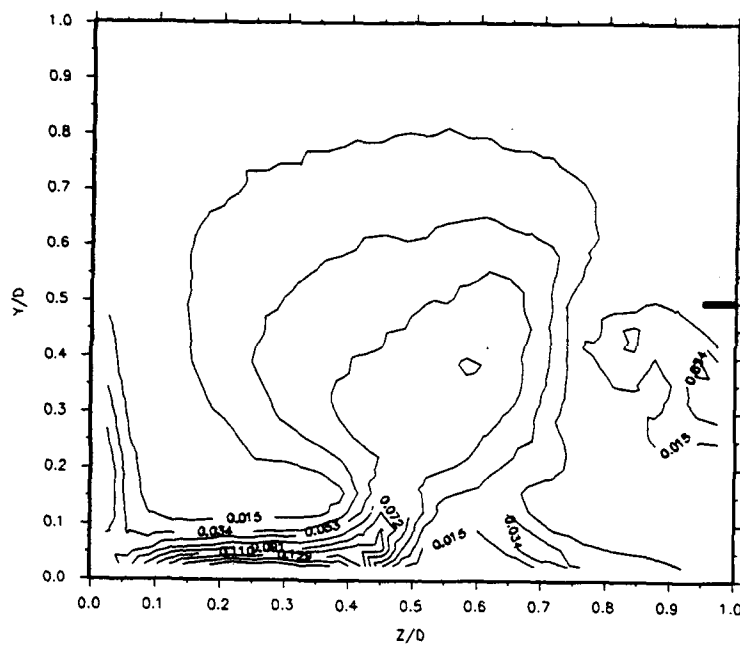
Figure 16: (cont.)

(e) 1.0 mm wide, full-length, half-height fence
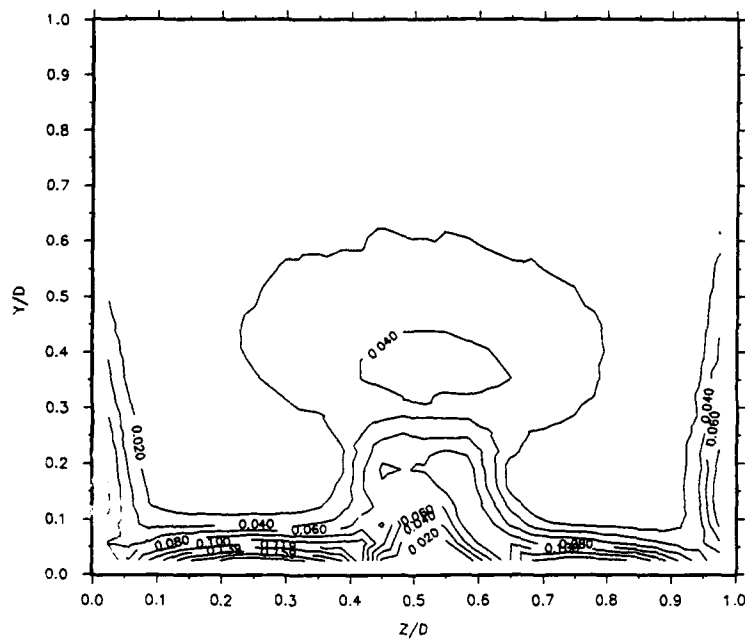
(f) no fence

Figure 16: (cont.)
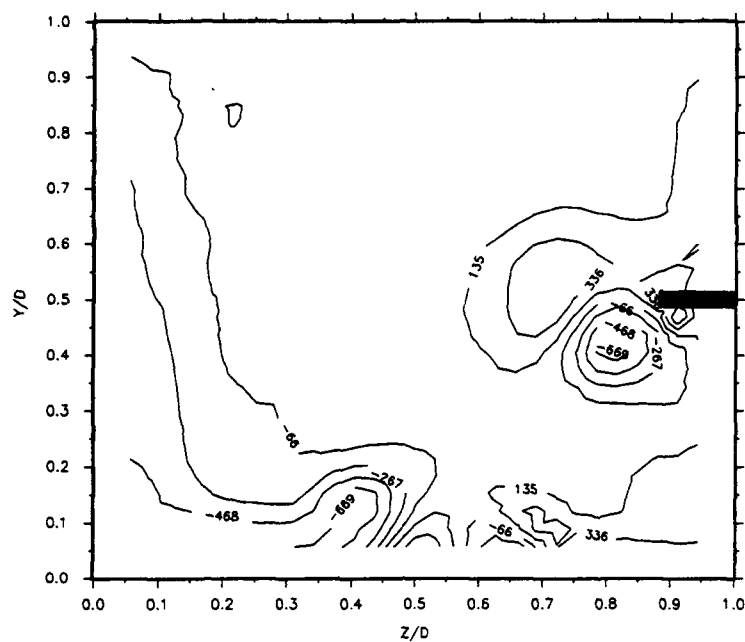
(a) 4.7 mm wide, full-length, full-height fence

(b) 4.7 mm wide, full-length, half-height fence

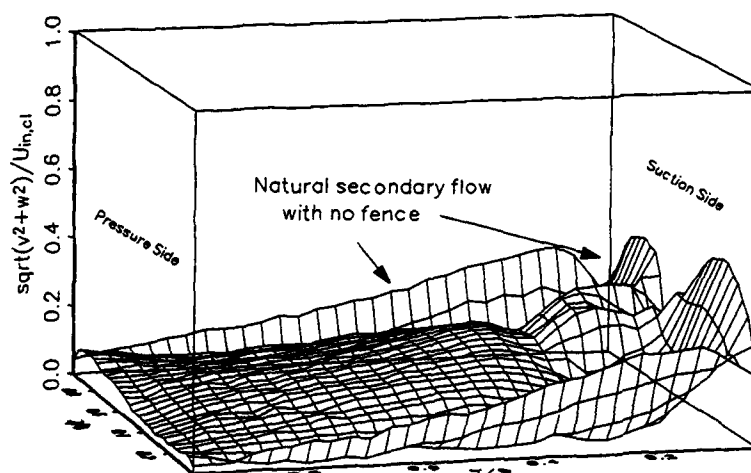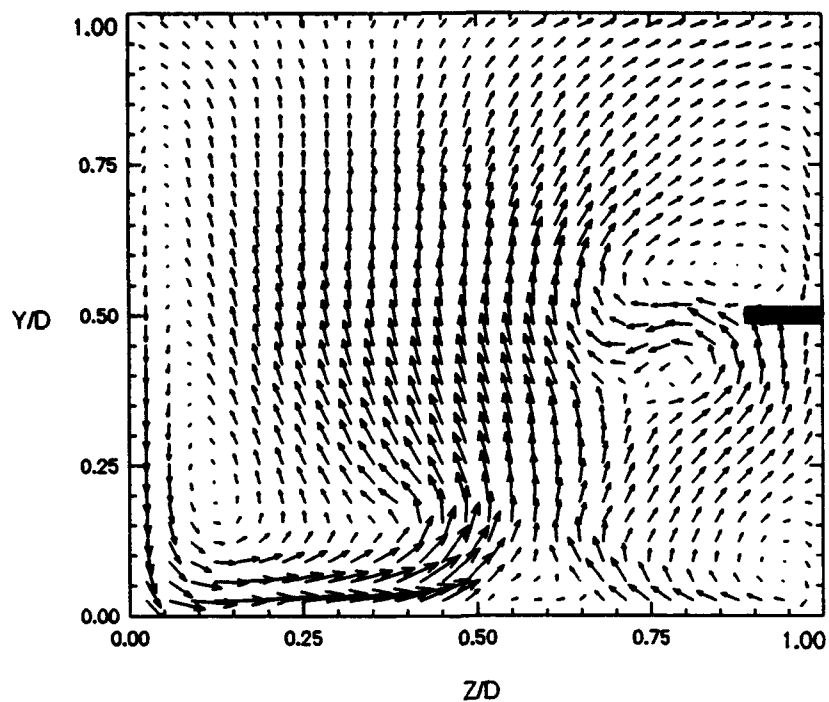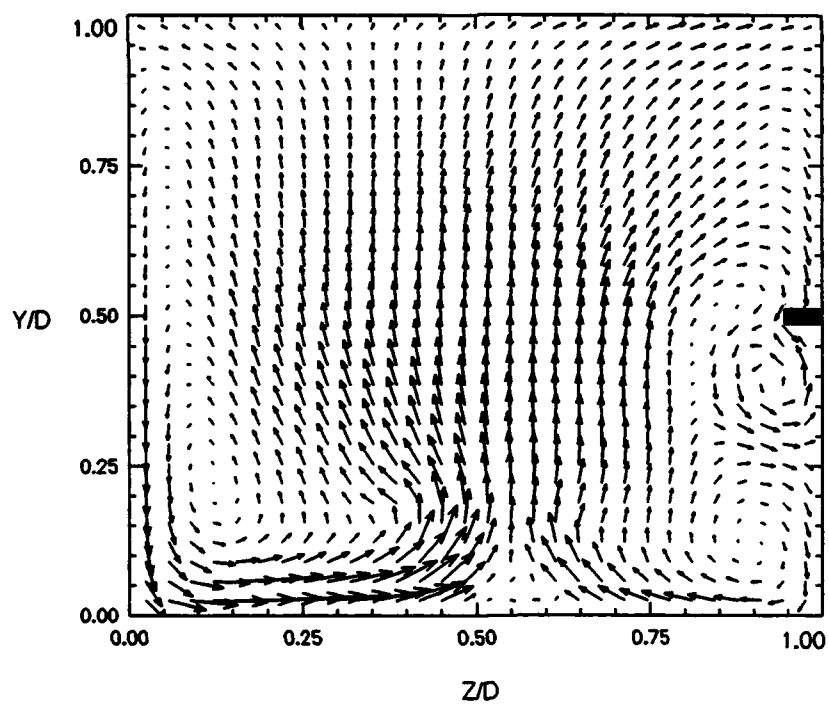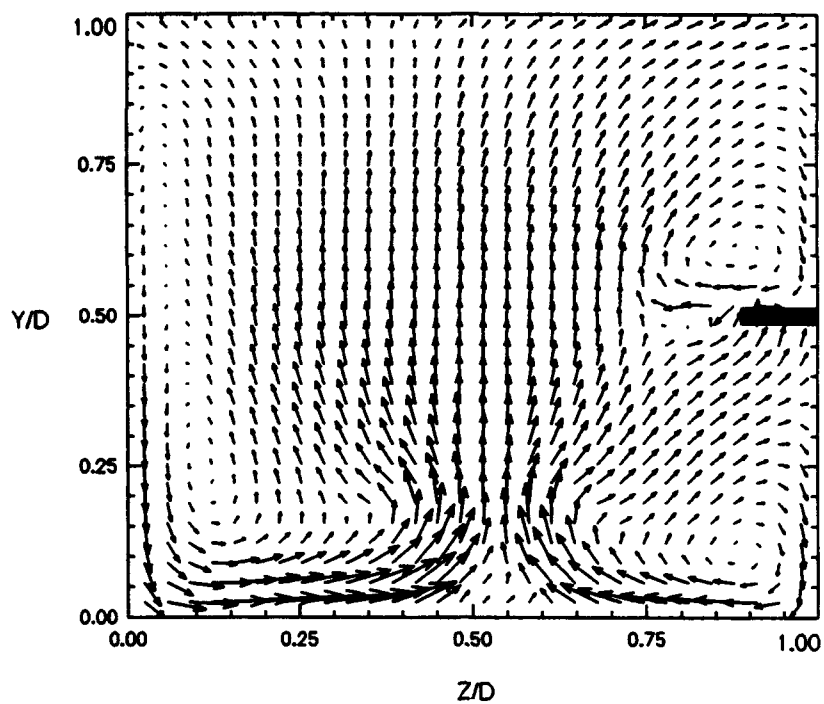Figure 17: Mean streamwise vorticity, ω_x, 90° plane   (cont. on next page)

(c) 4.7 mm wide, half-length, full-height fence

(d) 4.7 mm wide, half-length, half-height fence

Figure 17: (cont.)

(e) 1.0 mm wide, full-length, half-height fence
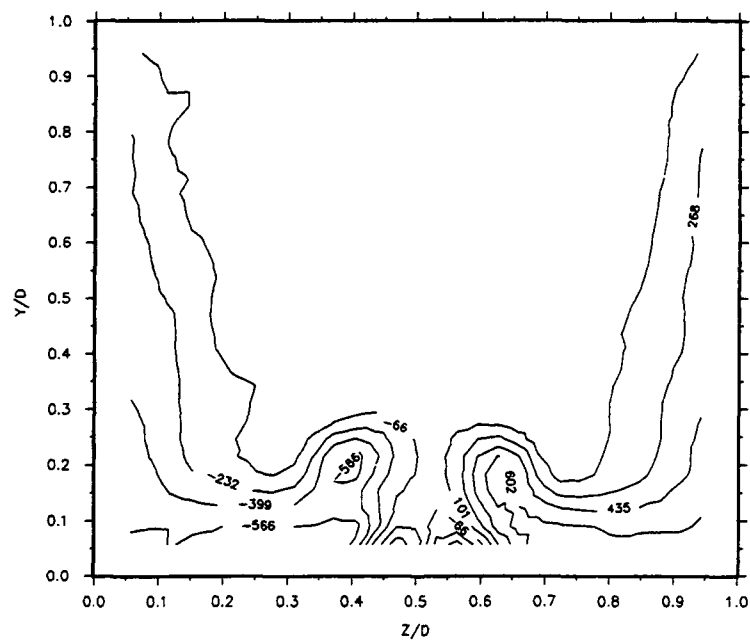
(f) no fence

Figure 17: (cont.)
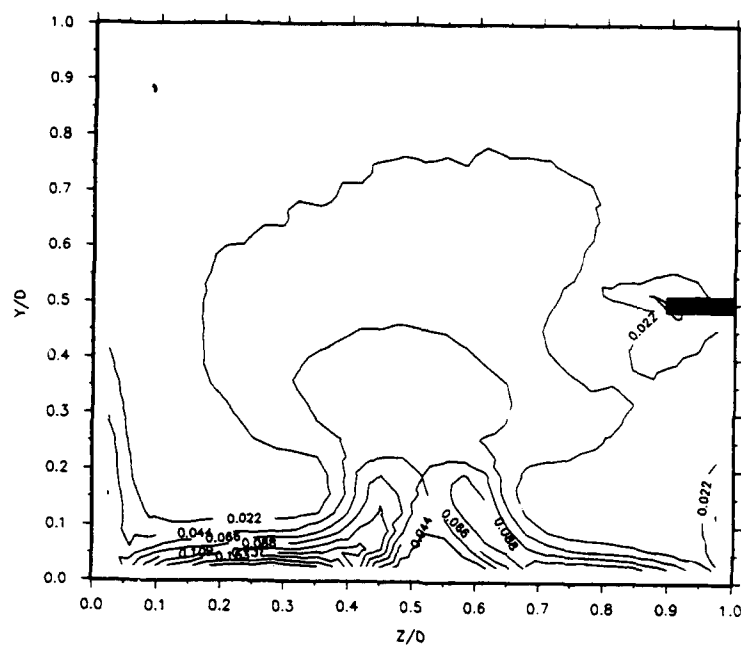
no-fence duct that convects low-energy boundary layer fluid from pressure to suction side along the endwall. Especially noteworthy are the high magnitude negative streamwise vortices near the endwall in Figures 17(b) and 17(e). These are the fence cases used for the endwall heat transfer investigation. The magnitude of streamwise vorticity along the fence endwall has decreased for all cases except in the region of negative vorticity. The total mean vorticity, Figure 18, has decreased, in general, along the fence endwall for all full-length fences except in the region of negative streamwise vorticity. Specifically, the thick and thin full-length fences show total vorticity reduction along the endwall of over 50% in the regions outside the negative streamwise vortex.

4.4. Endwall Heat Transfer

Endwall heat transfer measurements were made of one thick fence configuration, case (b), and the thin fence configuration, case (e). These measurements are compared with the endwall heat transfer measurements of the no-fence duct, Figure 19(a), presented in Wiedner and Camci (1993b). Color plots of the three cases greatly assist in portraying trends in heat transfer level and distribution and are shown in Figure 20. Purple represents low heat transfer levels and red is the highest convective heat transfer.

4.4.1. Thick Fence

The endwall heat transfer coefficient distribution for the 4.7mm wide, full-length, half-height fence is shown in Figure 19(b). At 0° h increases from pressure to suction side. The fence is evident at 5° as a dividing line between a region "above" (toward the outer radius) and "below" (toward the inner radius). From 5° to 30°, both above and below the fence, accelerating flow in the freestream corresponds to locally lower h value. Below the fence, though, is a full-contour level greater than above the fence. Heat transfer levels increase radially toward the higher pressure side of the two regions. Another noticeable feature from 5° to 45° is the line of constant h running from near the fence leading edge to the suction side that could correspond to any vortex coming off the fence leading edge. The only gradient in h present at 45° is the distinct change across the fence decreasing 27% on average from suction side to pressure side. A large area of maximum h level (solid triangles) is found between mid-passage and the suction side and remains fairly constant. This corresponds to the downwash region of the counter rotating vortices near the endwall in Figure 15(b). Above the fence, h increases continuously from 45° to 90°. This is associated with a favorable streamwise pressure gradient in the region above the fence as found in Wiedner and Camci (1993b). Very close to the exit plane the regions above and below the fence look very similar in distribution and magnitude. Maximum h levels are found in the center of both regions with decreasing h toward the fence and toward the pressure and suction sides. The maximum heat transfer in the duct at 90° is between mid-passage and the pressure surface.
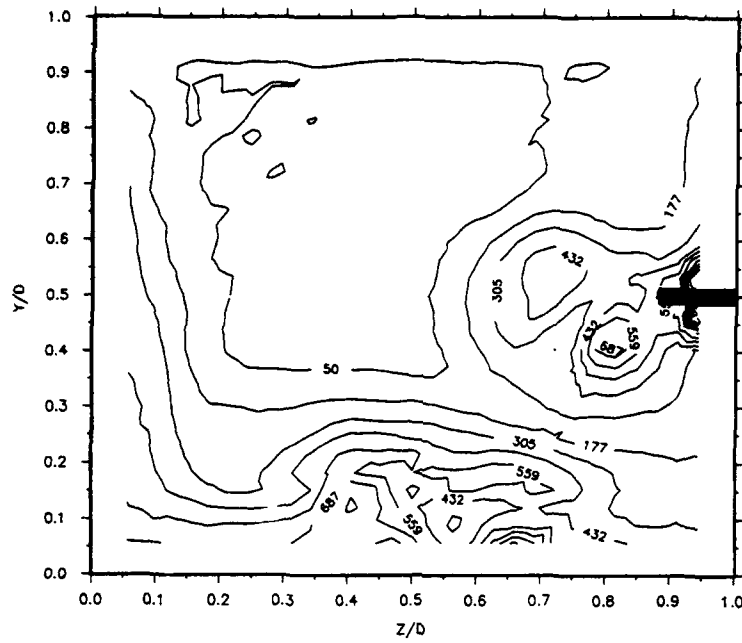
(a) 4.7 mm wide, full-length, full-height fence
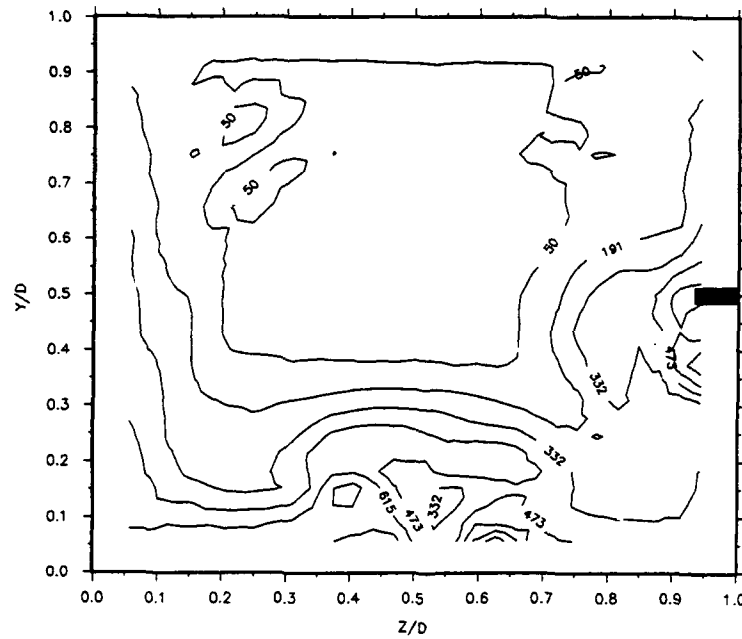
(b) 4.7 mm wide, full-length, half-height fence

Figure 18: Mean total vorticity, Ω, 90° plane   (cont. on next page)
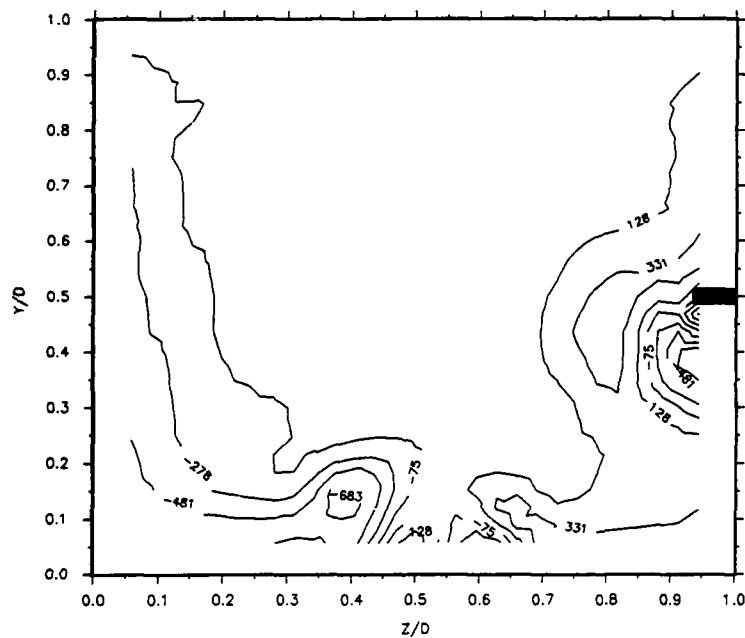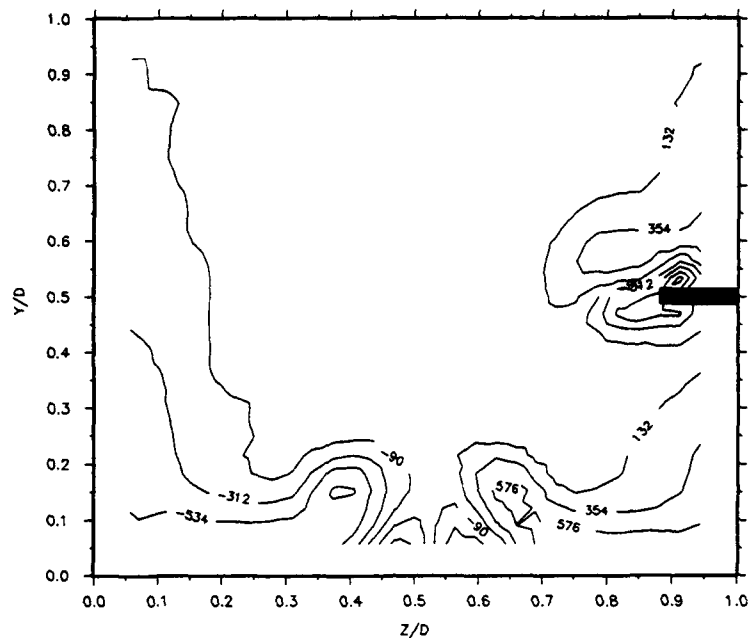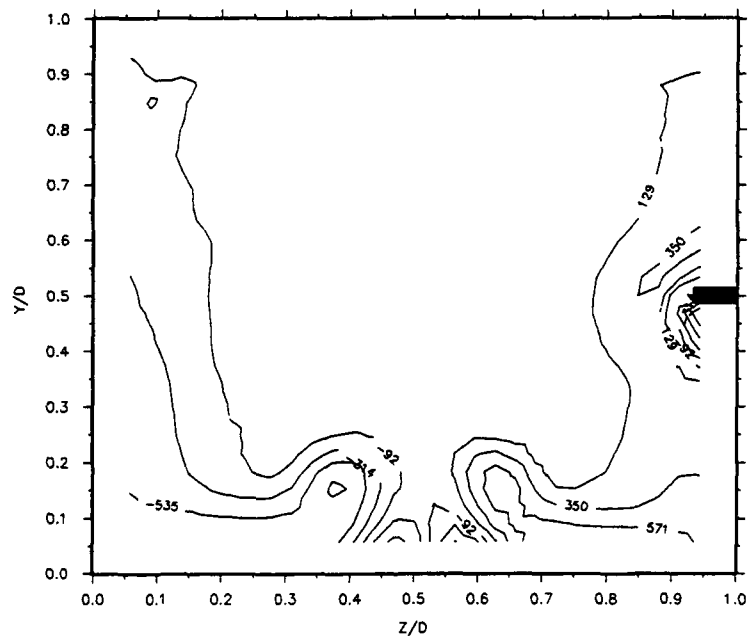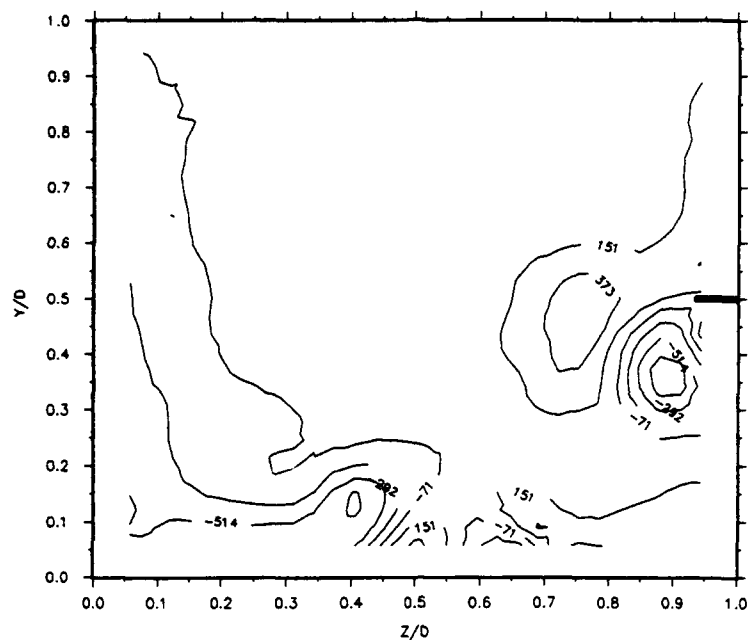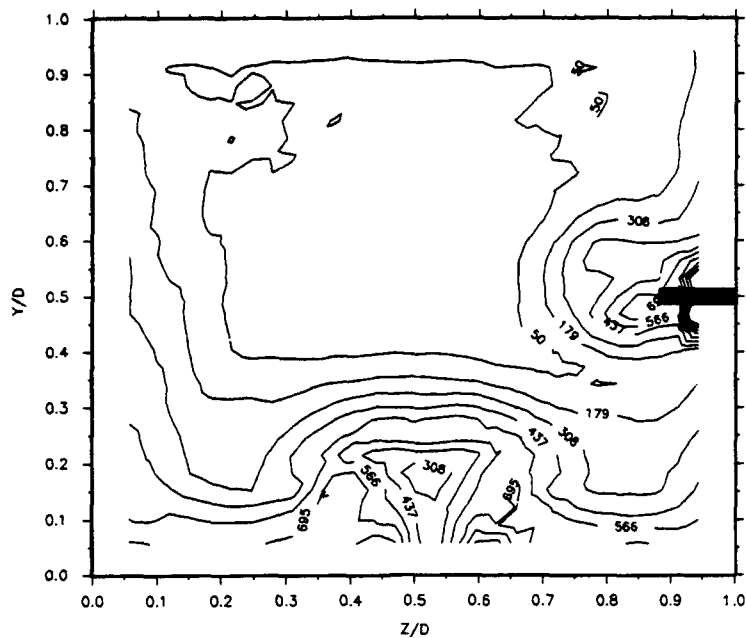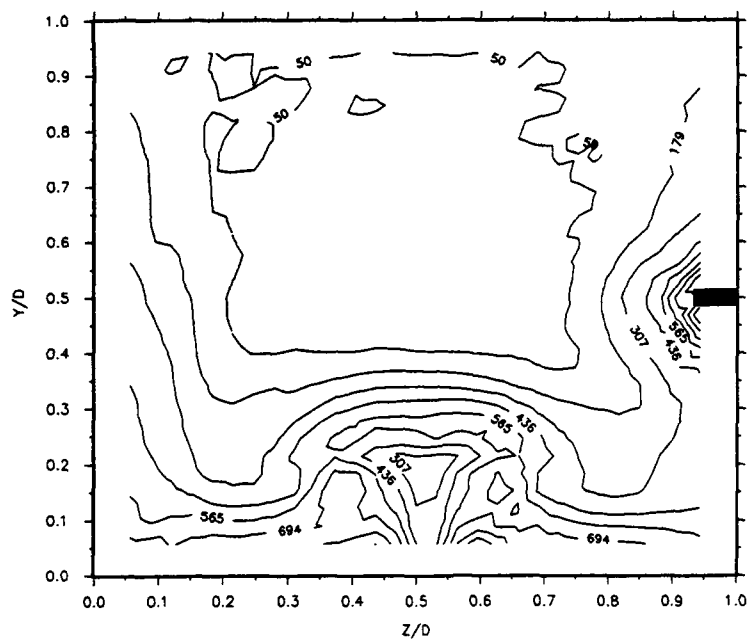
(c) 4.7 mm wide, half-length, full-height fence


(d) 4.7 mm wide, half-length, half-height fence
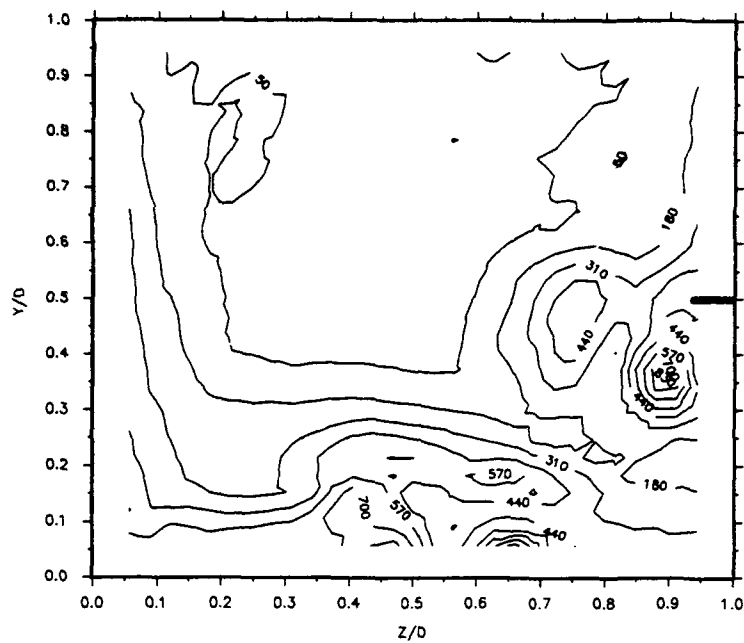
Figure 18: (cont.)

(e) 1.0 mm wide, full-length, half-height fence
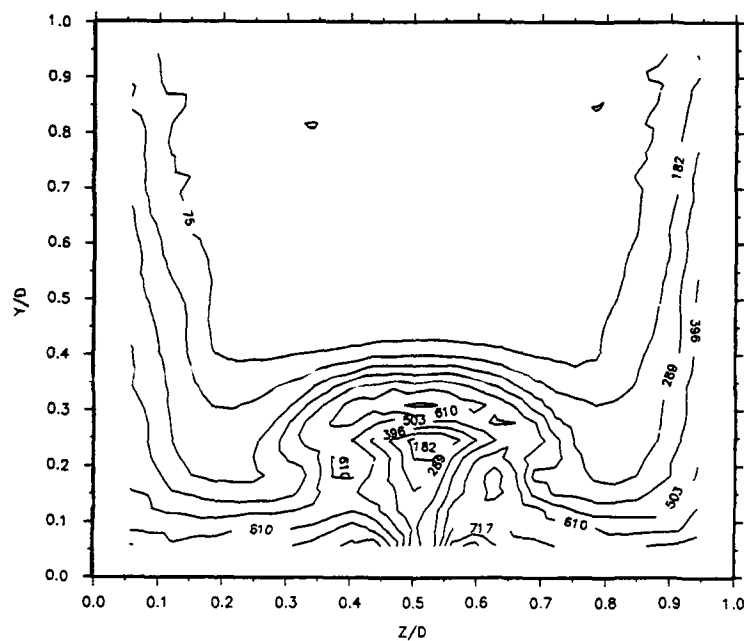
(f) no fence

Figure 18: (cont.)

4.4.2. Comparison of Thick Fence and No Fence

The thick fence has changed the magnitude and distribution of h in many areas of the duct when compared to the no-fence duct. The least amount of change is from 0° to 30° where many of the gross patterns are the same and levels are within 10% of each other. Minimum h levels in both cases are found between mid-passage and the duct pressure surface from 0° to 25°. The thick fence case shows significant effect of the mid-passage fence as the radial demarcation line between h levels that are 27% different. The difference in radially maximum and minimum h values at 45° for the no-fence case is 15-20%. Maximum h levels are present in both cases in the area between mid-passage and the suction surface from 50° to 80°. The thick fence case maximum h level is approximately 17% greater than the maximum h level in the no-fence case. Also similar is that h generally increases from pressure to suction side for 45° to 75°, though there are local decreases near the fence.

4.4.3. Thin Fence

The endwall h distribution for the 1.0mm wide, full-length, half-height fence is shown in Figure 19(c). At 0° h increases from pressure to suction side. Again at 5° the fence divides the duct endwall into two regions above and below the fence. The h levels for the thin fence case are consistently 10-15% greater than the thick fence levels for 0° to 30°. The h distribution at 45° is significantly different compared to the thick fence. The fence no longer serves as a definitive line between two regions. The difference in radially maximum and minimum h values at 45° is 25-30% like the thick fence case, but the gradients are steeper. The differences between thin and thick fence cases continue in the region from 45° to 90°. The fence again becomes a distinctive radial demarcation in the h distribution of the thin fence. Maximum h level is found between mid-passage and the suction surface, but is 10% greater then the thick fence case. This coincides with the downwash region of the counter rotating vortices near the endwall shown in Figure 15(e).

4.4.4. Comparison of Thin Fence and No Fence

The reduction in fence-side passage vortex results in endwall h distribution similar to the no-fence case, but with magnitudes uniformly greater. At 0° the thin fence h levels are consistently 10-15% greater than the no-fence case. At 50° into the turn the h values are 20% greater and up to 30% greater than the no-fence case in the region of maximum heat transfer between fence and suction surface from 50° to 80°. Distributions for the thin fence and no-fence cases show the same gross features radially and streamwise. Minimum h levels in both cases are found between mid-passage and pressure surface from 0° to 25°. Maximum h levels in both cases are found between mid-passage and suction surface from 50° to 80°.
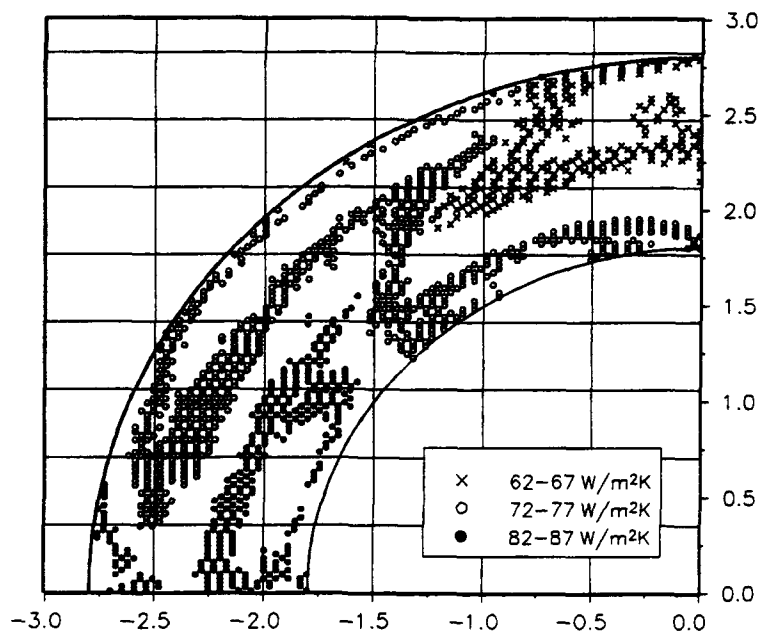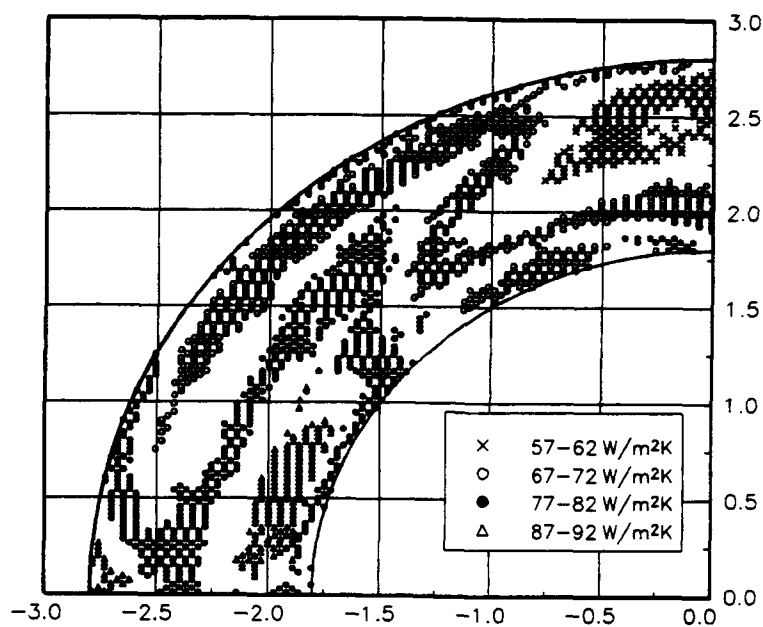
(a) no fence (from Wiedner and Camci, 1993b)

Figure 19: Endwall convective heat transfer coefficient contour plots   (cont. on next page)
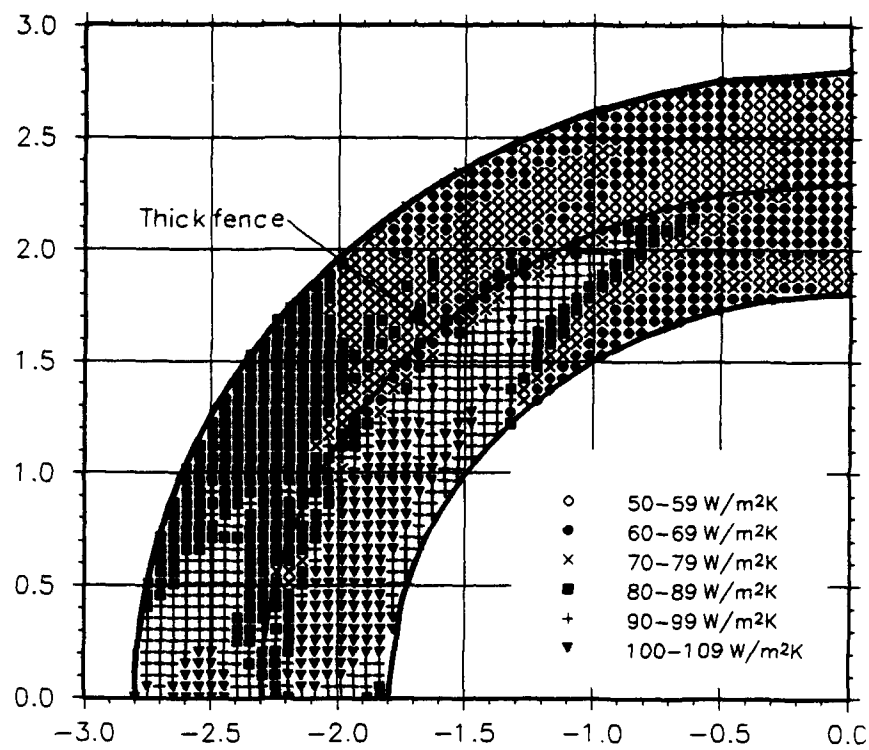
(b) 4.7 mm wide, full-length, half-height fence
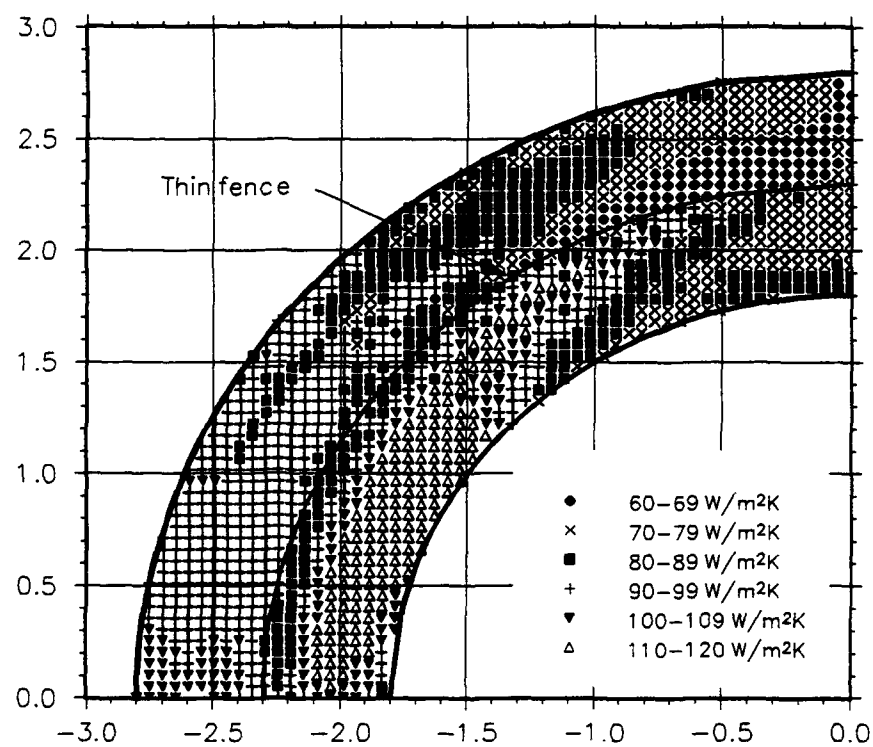
(c) 1.0 mm wide, full-length, half-height fence

Figure 19: (cont.)
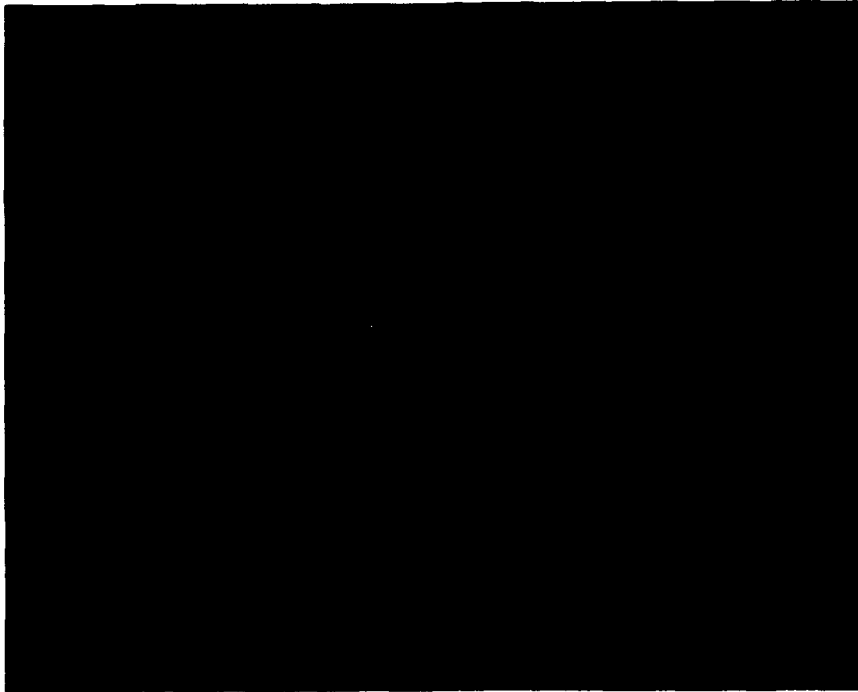
(a) no fence (from Wiedner and Camci, 1993b)

(b) 4.7 mm wide, full-length, half-height fence

Figure 20: Endwall convective heat transfer coefficient color plots   (cont. on next page)

(c) 1.0 mm wide, full-length, half-height fence

Figure 20: (cont.)

Chapter 5

CONCLUSIONS AND RECOMMENDATIONS

The aerodynamic and heat transfer effects are presented for six different configurations of a single endwall boundary layer fence in a 90° turning square duct. The fence dimensions (width, length, and height) are varied, but all fences are attached to the endwall midway between pressure and suction surfaces. A five-hole probe is used to measure the pressure and velocity fields at the 90° plane to identify secondary flow features and estimate aerodynamic losses. High resolution liquid crystal thermography is used to determine the convective heat transfer coefficient for the entire endwall surface for two fence configurations.

5.1. Fence Effects on Secondary Flow

1. The full-length fences decrease secondary flow along the endwall the most and also have the largest regions of total pressure loss near the endwall. This is evidence that the fences reduce the amount of low-energy boundary layer fluid that is convected by the passage vortex to the suction surface and that low-energy fluid remains near the endwall.

2. Half-height fences produce a pair of counter rotating vortices between the fence and the suction surface. Full-height fences act as blades and form two separate passage vortices near the endwall between the fence pressure and suction surfaces and the duct pressure and suction surfaces.

3. All fences show interaction of a vortex (of varying strength) on the endwall at $Y/D = .15-.35$, between the fence and suction surface, which is associated with the region of maximum heat transfer on the duct endwall.

4. All half-height fences reduce the passage averaged total pressure loss measured at 90° compared to the no-fence duct in agreement with the results of Kawai et al. (1989) for a cascade. The 4.7 mm wide, 12.7 mm high, 0°-90° long fence achieved the maximum passage averaged reduction of 6.5% of the no-fence value.

5. Fence dimensions can be optimized due to a trade-off between added viscous and mixing losses due to the fence and the reduction in losses due to a weakened passage vortex.

5.2. Heat Transfer

1. The boundary layer fence influenced the level of convective heat transfer coefficient rather than its distribution on the endwall. In the passage 0°-30° the fence separated the endwall into two regions with greater heat transfer between mid-passage and the suction side. Minimum h levels in both fence cases and the no-fence case were found between mid-passage and the pressure surface from 0° to 25°.

2. Both the thick and the thin fence increased the endwall heat transfer throughout the bend. Heat transfer enhancement was greatest for the thin (1.0mm wide), full-length (0°-90°), half-height (1/2 the inlet boundary layer thickness) fence positioned at mid-passage achieving an enhancement of 20% at 50°. Endwall heat transfer was enhanced up to 30% in the region of maximum heat transfer between fence and suction surface from 50° to 80°. The blockage effect of the fence wake may account for some of the heat transfer enhancement due to increased local velocity magnitudes near the endwall.

3. The increasing heat transfer levels for both fence cases and the no-fence duct between mid-passage and the pressure surface from 45° to 90° coincides with a favorable streamwise pressure gradient.

4. The maximum heat transfer levels seen in both fence cases coincides with the downwash region of counter rotating vortices formed near the endwall between fence and suction surface. Maximum heat transfer levels in all cases were found between mid-passage and suction surface from 50° to 80°.

5.3. Recommendations

The role of turbulence in the secondary flow features induced by the endwall fence and in the heat transfer to the endwall is a reasonable next step in this investigation. The author recommends the measurement of fluctuating components of velocity in the endwall boundary layer at several streamwise locations with a fence installed to determine if turbulent to laminar transition occurs and its role in endwall heat transfer. Any investigation of fence effects on the turbulent boundary layer structure could be completed in the same duct as the present study. Another recommendation is to build a 90° rectangular duct with width (span) greater than height (pitch) that converges slowly through the turn. The converging 90° rectangular duct would allow further low-cost studies of endwall boundary layer fences while more closely simulating the flow acceleration found in a turbine passage and using much of the same equipment and facilities required for the present study.

REFERENCES

Abernathy, R.B., Benedict, R.P. and Dowdell, R.B., 1985, "ASME Measurement Uncertainty," *ASME Journal of Fluids Engineering*, Vol.107, pp.161-164.

Blair, M.F., 1974, "An Experimental Study of Heat Transfer and Film Cooling on Large Scale Turbine Endwalls," *Journal of Heat Transfer*, Vol. 96, pp. 524-529.

Boyle, M.T. and Hoose, K.V., 1989, "Endwall Heat Transfer in a Vane Cascade Passage and in a Curved Duct," 89-GT-90, Presented at the Gas Turbine and Aeroengine Congress and Exposition, Toronto, Canada, June.

Boyle, M.T., Simonds, M. and Poon, K., 1988, "A Comparison of Secondary Flow in a Vane Cascade and a Curved Duct," ASME HTD-Vol.103, Heat Transfer in Gas Turbine Engines and Three Dimensional Flows, pp. 85-93.

Boyle, R.J. and Russell, L.M., 1989, "Experimental Determination of Stator Endwall Heat Transfer," *Journal of Turbomachinery*, Vol. 112, pp. 547-558.

Camci, C., 1989, "An Experimental and Numerical Investigation of Near Cooling Hole Heat Fluxes on a Film Cooled Turbine Blade," *ASME Journal of Turbomachinery*, Vol. 111, pp. 63-70.

Camci, C., Kim, K. and Hippensteele, S. A., 1992, "A New Hue Capturing Technique for the Quantitative Interpretation of Liquid Crystal Images Used in Convective Heat Transfer Studies," *ASME Journal of Turbomachinery*, Vol. 114, pp. 765-775.

Chung, J.T., Simon, T.W. and Buddhavarapu, J., 1991, "Three-Dimensional Flow near the Blade/Endwall Junction of a Gas Turbine: Application of a Boundary Layer Fence," ASME Paper 91-GT-45, presented at the 36th ASME International Gas Turbine and Aeroengine Congress and Exposition.

Chung, J.T. and Simon, T.W., 1993, "Effectiveness of the Gas Turbine Endwall Fences in Secondary Flow Control at Elevated Freestream Turbulence Levels, " 93-GT-51, Presented at the International Gas Turbine and Aeroengine Congress and Exposition, Cincinnati, Ohio, May.

Cooper, T.E., Field, R.J. and Meyer, J.F., 1975, "Liquid Crystal Thermography and Its Application to the Study of Convective Heat Transfer," *Journal of Heat Transfer*, August, pp. 442-449.

Fergason, J.L., 1968, "Liquid Crystals in Nondestructive Testing," *Applied Optics*, Vol. 7, pp. 1729-1737.

Fisher, E.M. and Eibeck, P.A., 1990, "The Influence of a Horseshoe Vortex on Local Convective Heat Transfer," *ASME Journal of Heat Transfer*, Vol. 112, pp. 329-335.

Gaugler, R.E. and Russell, L.M., 1984, "Comparison of Visualized Turbine Endwall Secondary Flows and Measured Heat Transfer Patterns," *ASME Journal of Engineering for Gas Turbines and Power*, Vol. 106, pp. 168-172.

Goldstein, R.J. and Spores, R.A., 1988, "Turbulent Transport on the Endwall in the Region Between Adjacent Turbine Blades," *ASME Journal of Heat Transfer*, Vol. 110, pp. 862-869.

Graziani, R.A., Blair, M.F., Taylor, J.R. and Mayle, R.E., 1980, "An Experimental Study of Endwall and Airfoil Surface Heat Transfer in a Large Scale Turbine Blade Cascade," *ASME Journal of Engineering for Power*, Vol. 102, pp. 257-267.

Gregory-Smith, D.G., Graves, C.P. and Walsh, J.A., 1988, "Growth of Secondary Losses and Vorticity in an Axial Turbine Cascade," *ASME Journal of Turbomachinery*, Vol. 110, pp. 1-8.

Hippensteele, S.A. and Russell, L.M., 1988, "High-Resolution Liquid-Crystal Heat-Transfer Measurements on the End Wall of a Turbine Passage With Variations in Reynolds Number," NASA TM 100827.

Kawai, T., Shinoki, S. and Adachi, T., 1989, "Secondary Flow Control and Loss Reduction in a Turbine Cascade Using Endwall Fences," *JSME International Journal*, Series II, Vol. 32, No.3, pp. 375-387.

Kinnear, I.S., May, A.L. and Wall, R.A., 1980, "Secondary Flow Control in Axial Fluid Flow Machine," UK Patent Application GB 2 042 675 A.

Langston, L.S., 1980, "Crossflows in a Turbine Cascade Passage," *ASME Journal of Engineering for Power*, Vol. 102, pp. 866-874.

Langston, L.S., Nice, M.L. and Hooper, R.M., 1977, "Three-Dimensional Flow within a Turbine Cascade Passage," *ASME Journal of Engineering*, Vol. 99, pp.21-28.

Mayle, R.E., 1991, "The Role of Laminar-Turbulent Transition in Gas Turbine Engines," *ASME Journal of Turbomachinery*, Vol. 113, pp. 509-537.

Pauley, W.R. and Eaton, J.K., 1988, "The Fluid Dynamics and Heat Transfer Effects of Streamwise Vortices Embedded in a Turbulent Boundary Layer," Report MD-51, Thermosciences Division, Department of Mechanical Engineering, Stanford University.

Prumper, H., 1972, "Application of Boundary Layer Fences in Turbomachinery," AGARDograph #164, pp. 311-331.

Sharma, O.P. and Butler, T.L., 1987, "Predictions of Endwall Losses and Secondary Flows in Axial Flow Turbine Cascades," *ASME Journal of Turbomachinery*, Vol. 109, pp. 229-236.

Sharma, O.P. and Graziani, R.A., 1983, "Influence of Endwall Flow on Airfoil Suction Surface Midheight Boundary Layer Development in a Turbine Cascade," *ASME Journal of Engineering for Power*, Vol. 105, pp. 147-155.

Sieverding, C.H., 1985, "Recent Progress in the Understanding of Basic Aspects of Secondary Flows in Turbine Blade Passages," *ASME Journal of Engineering for Gas Turbines and Power*, Vol. 107, pp. 248-257.

Sitaram, N., Laksminarayana, B. and Ravindranath, A., 1981, "Conventional Probes for the Relative Flow Measurements in a Turbomachinery Rotor Blade Passage," *Journal of Engineering for Power*, Vol. 103, pp. 406-414.

Taylor, A.M.K.P., Whitelaw, J.H. and Yianneskis, M., 1982, "Curved Ducts With Strong Secondary Motion: Velocity Measurements of Developing Laminar and Turbulent Flow," *ASME Journal of Fluids Engineering*, Vol. 104, pp. 350-359.

Treaster, A.L. and Yocum, A.M., 1979, "The Calibration and Application of Five-hole Probes," *ISA Transactions*, Vol. 18, No.3, pp. 23-34.

Weidner, B.G. and Camci, C., 1993a, "A Technique for the Determination of Local Heat Flux on Steady State Heat Transfer Surfaces with Arbitrarily Specified External and Internal Boundaries," Proceedings of the 1993 National Heat Transfer Conference, Atlanta, Georgia, August.

Weidner, B.G. and Camci, C., 1993b, "Passage Flow Structure and its Influence on Endwall Heat Transfer in a 90° Turning Duct: Mean Flow and High Resolution Endwall Heat Transfer Experiments," 93-WA/HT-52, Presented at the ASME Winter Annual Meeting, New Orleans, Louisiana, November.

Appendix

EXPERIMENTAL UNCERTAINTY ANALYSIS

Sources of error for five-hole probe and heat transfer measurements are discussed and calculated values of uncertainty are presented in this appendix. Uncertainty levels for measured and derived values have been estimated using the procedure of Abernathy et al. (1985). Table 2 summarizes the results based on 20:1 odds. Uncertainty levels are not constant across an entire measurement plane. The values in Table 2 represent averages of the uncertainty calculated at each point in the measurement grid.

TABLE 2: EXPERIMENTAL UNCERTAINTY

Aerodynamic Data	Uncertainty*
$U_{95}(U/U_{in,cl})$	$\pm .0114$
$U_{95}(\sqrt{(V^2+W^2)}/U_{in,cl})$	$\pm .0026$
$U_{95}(C_{pt})$	$\pm .015$
$U_{95}(\Omega)$	$\pm 35\ (s^{-1})$

Heat Transfer Data	Precision (%)	Bias (%)	Uncertainty* (%)
$U_{95}(h)$	± 4.9	± 2.3	± 5.4
$U_{95}(q_{gen})$	± 3.2	$\pm .8$	± 3.3
$U_{95}(q_{cond})$	± 5.0	± 4.8	± 6.9
$U_{95}(q_{rad})$	± 1.8	± 15.7	± 15.8
$U_{95}(T_\infty)$	± 1.0	± 1.2	± 1.6
$U_{95}(T_w)$	$\pm .14$	$\pm .28$	$\pm .3$

*using root-sum-of-the-squares combination of precision and bias uncertainties

A.1. Five-hole Probe Measurements

Sources of error for the five-hole probe measurements included Reynolds number variation, wall proximity effects, probe blockage and probe stem effects, turbulence effects, displacement effect, spatial error, probe misalignment, pressure loss in the connections, and extrapolation and interpolation error. Each of these sources are discussed.

A.1.1. Effect of Reynolds Number Variation

Trester and Yocum (1979) found that an angle-tube type five-hole probe, such as the probe used in this study, has a measurable change in the static pressure coefficient, $C_{p,static}$, for a variation in the flow Reynolds number. The other three probe coefficients, $C_{p,total}$, $C_{p,yaw}$, and $C_{p,pitch}$, were essentially unaffected. The five-hole probe in this study was calibrated at the same Reynolds number as the experimental test runs and this source of error was considered negligible.

A.1.2. Wall Proximity Effect

Treaster and Yocum (1979) suggest that wall proximity effects on the five-hole calibration data are reduced if the probe is restricted to distances greater than two probe diameters from the wall. For this study, the probe measurement grid was 5 mm from the wall, greater than three probe diameters, and this source of error was considered negligible.

A.1.3. Effects of Probe Blockage and Probe Stem

The probe effectively blocks the flow when it is inserted into the duct to take measurements. This blockage induces increased streamwise velocity and ranges from approximately 0% to less than 1.5% of the cross sectional area at the greatest probe insertion depth. This source of error is incorporated into the uncertainty value in Table 2 according to the method of Abernathy et al. (1985).

The effect of the probe stem interfering with the flow near the probe tip is discussed in Sitaram et al. (1981). They found that this effect is negligible when the distance between the probe tip and the axis of the stem is more than four times the stem diameter. The probe tip is four times the stem diameter from the stem axis for the probe used in this study and this source of error is considered negligible.

A.1.4. Turbulence Effect

The probe measurements in the actual duct flow field were taken at turbulence intensity levels much greater than the uniform flow in which the probe was calibrated. This source of error is called turbulence effect and is discussed in Sitaram et al. (1981). They conclude that the estimated error in total velocity is approximately 0.33% and the estimated error in pressures and angles is .67% in the region of 10% turbulence intensity. No turbulence measurements were made in this study, but based on the inlet boundary layer turbulence levels these estimates of error due to turbulence are assumed for this study. This was incorporated into the determination of uncertainty as a bias error according to the method of Abernathy et al. (1985).

A.1.4. Displacement Effect

The displacement effect refers to the probe indicating a measurement at a location different from

geometric center of the probe. Sitaram et al. (1981) estimate this error using Equation A.1.

$$\delta = .021 \, d_h \tag{A.1}$$

where δ is the displacement of the probe measuring point from the geometric center and d_h is the diameter of the probe holes. This corresponds to 0.1% of the distance between points in the 30 x 30 measurement grid and is considered negligible.

A.1.6. Spatial Error

There is a source of error in five-hole probe measurements due to each hole being located in different pressure fields in steep pressure and velocity gradients such as found in boundary layers. This is called spatial error and is estimated by Sitaram et al. (1981) using Equation A.2.

$$\epsilon = 13.2 \, \frac{d}{P_1} \, (\frac{dP_1}{dn}) \tag{A.2}$$

where ϵ is the error in degrees, d is the probe head diameter, and P_1 is the pressure by the hole at the geometric center of the probe. The small diameter probe used in this study reduced this error. This source of error was incorporated into the determination of uncertainty as a bias error.

A.1.7. Probe Misalignment

The probe was aligned with the side walls of the duct using a ruler. The bias error was estimated to be $\pm$ 0.5 degree and was incorporated into the determination of uncertainty.

A.1.8. Pressure Loss in the Connections

This source of error was considered negligible since all connections were maintained from the time of calibration through the entire experiment except the connections between the probe and the pressure transducers. Any pressure lost was assumed to be accounted for in the calibration of the five-hole probe and the pressure transducers.

A.1.9. Extrapolation Error

The error due to extrapolation on the five-hole probe calibration maps was considered negligible. The probe was calibrated in the range of $\pm$ 30 degrees in pitch and yaw angle and no flow measurements exceeded 25 degrees. Error due to interpolation of the five-hole probe calibration maps was incorporated in the determination of uncertainty as a precision error.

A.2. Heat Transfer Measurements

Sources of error for the heat transfer measurement included thermocouple film and probe inaccuracy, liquid crystal calibration, finite element code calculation of generated heat flux, infrared thermometer inaccuracy, and errors in heat flux lost to conduction and radiation. Uncertainty in the calculated convective heat transfer coefficient is mainly due to the comparatively small amounts of conductive and radiative losses and the small uncertainty in the finite element calculation of the generated heat flux. The two-dimensional technique used to estimate radiative losses led to the greater levels of uncertainty in that value shown in Table 2.

A.2.1. Thermocouple Film and Probe Inaccuracy

The k-type, thin film thermocouples mounted on the duct endwall for liquid crystal calibration were calibrated against a laboratory quality mercury thermometer in a water bath. Precision and bias errors gained from this calibration were incorporated into the calibration of the liquid crystals. The k-type thermocouple probe was calibrated against the same mercury thermometer in the duct freestream flow. A recovery factor of 1 was assumed due to the relatively slow velocity of the flow. The precision and bias errors of the probe calibration were incorporated into the uncertainty of the heat transfer coefficient value as error in freestream temperature according to the method of Abernathy et al. (1985).

A.2.2. Liquid Crystal Calibration

The spatial and temporal averaging used in the liquid crystal calibration as described in Chapter 3 reduced the error introduced by the liquid crystals. Precision and bias error determined from the calibration were incorporated into the determination of uncertainty of derived values as error in the wall temperature.

A.2.3. Finite Element Code Calculation of Generated Heat Flux

The finite element computer code is very accurate. A small bias error in generated heat flux was assumed due to possible variations in foil conductivity and thickness. Precision and bias error were incorporated into the determination of the uncertainty in the heat transfer coefficient.

A.2.4. Infrared Thermometer Inaccuracy

The infrared thermometer was calibrated against the same mercury thermometer as the other temperature measurement devices. Precision error gained from this calibration and bias error gained from the manufacturer's specifications were incorporated into the determination of uncertainty as error in the derived value of heat flux lost to conduction.

A.2.5. Error in Heat Flux Lost to Conduction and Radiation

Uncertainty in the value of thermal conductivity of plexiglass, $k = .1875$ W/m K, and in the plexiglass thickness were incorporated into the uncertainty of the derived value of heat flux lost to conduction. As mentioned in Chapter 3, the effect of lateral conduction was discussed in Wiedner and Camci (1993b) and was considered negligible.

Uncertainty in the derived value of heat flux lost to radiation was mainly due to the large bias error assumed in the shape factors that were based on two-dimensional analysis. These errors in heat flux lost to conduction and radiation were incorporated in to the uncertainty of the derived value of heat transfer coefficient according to the method of Abernathy et al. (1985).